nature communications

Article

https://doi.org/10.1038/s41467-025-57934-z

High-speed computed tomography to visualise the 3D microstructural dynamics of oil uptake in deep-fried foods

Received: 13 June 2024

Accepted: 27 February 2025

Published online: 16 March 2025

Check for updates

U. Verma[1], I. M. Riley[2], B. Lukić[3], L. Broche[3], P. Verboven[1] ✉, J. A. Delcour[2] & B. M. Nicolaï[1,4]

Oil serves as both the high-temperature heating medium during deep-frying unit operations and a contributor to the organoleptic properties of deep-fried foods. Its absorption is linked to structural deformations during deep-frying that create pathways for oil to enter the food microstructure. This study proposes a 4D imaging system (three spatial dimensions and time) using fast synchrotron radiation tomography for in-situ visualisation during deep-frying and post-frying cooling to understand the mechanisms behind oil absorption. Using wheat flour dough as a model food system, we investigate the impact of frying oil temperature on structural deformation and pore formation in the crust and core, pore structure integrity, and oil uptake and distribution. The results show that higher temperatures lead to the formation of a distinguished crust with surface openings, facilitating greater oil absorption in small crust pores through capillary action. Comparing 3D microstructures attained at different frying oil temperatures, final oil content reaches 14.4% at 180 °C, 12.2% at 150 °C, and 1.3% at 120 °C, with temperature-dependent structural changes in pore connectivity and network integrity significantly impacting the rate of oil uptake and its distribution.

Deep-frying is a widely popular food processing technique in which foods are fully immersed in hot oil (150–180 °C). The applicability of this process to a large variety of food products and the distinct flavour and sensory characteristics imparted thereby have made deep-fried foods a staple in diets all over the world, particularly so for Western diets[1,2]. Deep-fried products based on wheat flour (ca. 70–75% starch and 10–12% protein) are popular across several product categories (e.g., donuts, noodles, breaded products) and culture-specific product variations within each category (e.g., the donut-style beignet in France, churros in Spain, youtiao in China) have made deep-fried foods based on wheat flour ubiquitous worldwide. These products, however, typically have a high fat content (ca. 10–35 g / 100 g portion) and thus, high energy density[3,4]. Numerous systematic reviews highlight a concerning association between the excessive caloric content in deep-fried products and detrimental health conditions associated with their (over-)consumption[5,6]. Moreover, the high temperatures involved in the deep-frying process facilitate chemical reactions that produce acrylamide, a compound classified as a probable human carcinogen, thereby raising potential health risks with regular consumption[7]. Current World Health Organisation (WHO) dietary guidelines recommend limiting total fat intake to 30% of the total energy intake[8]. Though obtaining deep-fried food products with desirable organoleptic characteristics and adequate nutritional profile remains a challenge for the food industry, it is ever so more essential as health-related issues associated with their consumption and scrutiny over processed food materials has continued to grow in recent years[9,10].

The structural properties of deep-fried porous food matrices develop during deep-frying (in part) due to the rapid phase conversion

[1]Division BIOSYST-MeBioS, KU Leuven, Willem de Croylaan 42, B-3001 Leuven, Belgium. [2]Laboratory of Food Chemistry and Biochemistry, KU Leuven, Kasteelpark Arenberg 20, B-3001 Leuven, Belgium. [3]European Synchrotron Radiation Facility, CS 40220, Grenoble F-38043, France. [4]Flanders Centre of Postharvest Technology, Willem de Croylaan 42, B-3001 Leuven, Belgium. ✉e-mail: pieter.verboven@kuleuven.be

of water to steam which causes gas cells to form and fill with steam. The consequent increase in internal pressure results in the expansion and deformation of the internal structure before steam eventually escapes at the surface[11,12]. The resulting porous solid matrix (hereafter referred as the microstructure) varies spatially across the fried product and features a broad distribution of pore volumes and thicknesses of the solid walls[13,14]. Although the mechanism(s) dictating and/or influencing oil absorption during and after the deep-frying process have been previously reported[2,4], the dynamics of these processes as well as their contribution to the final product oil content are still not fully understood. This is likely due to the highly complex and intense nature of the deep-frying process, as related to the rapid and simultaneous heat and mass transfer phenomena, which have made in-situ studies necessary to underpin the proposed hypotheses challenging.

Early studies regarded oil uptake purely as a surface phenomenon[4,15,16] and highlighted the importance of surface properties (e.g., surface roughness[17,18], geometry[19], permeability to oil[20,21]) in influencing adhesion of frying oil at the surface of deep-fried products[19]. Today, it is generally accepted that oil uptake is a pressure driven phenomenon. Positive internal pressures developing during water evaporation and product expansion inhibit oil ingress during deep-frying. During cooling, vapour condensation provides a favourable pressure gradient for the absorption of oil present on the surface of the food into the internal matrix[1]. Several experimental studies[16,22] and numerical models[12,23] focused on oil uptake dynamics have demonstrated oil ingress to primarily occur after removal from the frying oil. Additionally, oil uptake in the crust micropores has been ascribed to changes in capillary pressures, indicating the crucial role that the pore network morphology (e.g., porosity[22,24], pore size[25]) and in turn, microstructural changes during the deep-frying process, may have on the dynamics of oil absorption[26]. The extent of these microstructural changes depends on the product composition (e.g., moisture content[27]), starch and protein properties[28,29], and frying conditions (e.g., oil temperature[30], frying duration[2]). Recently, the relationship between product microstructure and oil-absorption during deep-frying has been investigated to better understand deep-frying induced oil absorption behaviour[14,28,31]. However, due to the previous inability to study the deep-frying process in real time, specific and direct relationships between the evolving 3D microstructure and oil uptake are currently lacking[15,30]. Establishing a link between these phenomena is deemed essential to further understand deep-frying induced oil absorption in food materials.

Wheat-flour dough (WFD) is formed by hydration of flour particles and kneading-induced mechanical stresses which lead to the development of a distinct cross-linked viscoelastic gluten network which surrounds starch granules and entraps gas pores (gas cells) therein[32]. The microstructural properties of deep-fried WFD-based foods are strongly related to the physicochemical changes and phase transitions (e.g., glass transition) of both starch and gluten proteins that occur during the process[28,32–35]. Starch granules swell and gelatinise during deep-frying, thereby exhibiting altered morphological properties (e.g., disruption and/or aggregation of granules)[35,36]. It has also been shown that deep-frying induced product deformation characteristics are strongly influenced by the gluten content, with WFD systems of higher gluten content exhibiting lower oil uptake[29]. Furthermore, the microstructural changes and oil uptake likely also depend on the moisture content[14,27].

Monitoring the microstructural changes of WFD-based systems during deep-frying and subsequent cooling can assist in linking the transformations taking place in this complex food formulation with oil absorption behaviour induced by the deep-frying process. State-of-the-art imaging techniques (optical light microscopy[37], scanning electron microscopy[25,38], confocal laser scanning microscopy[39,40]) have been extensively utilised for exploring the microstructure of deep-fried foods, analysing pore structure in crust and core regions, and locating oil inside these products[41,42]. Non-destructive imaging has become feasible using magnetic resonance imaging[43,44] and X-ray microcomputed tomography (μCT)[14,28,45], with the latter providing significantly higher spatial resolution to characterise the microstructure, although the dynamics of the process have never been captured completely[46]. The brilliance of synchrotron light sources enable μCT acquisitions at spatial and temporal resolutions that are magnitudes higher than those currently achievable in lab-based μCT settings[47]. 4D μCT imaging has been used at lower temporal resolutions to gain valuable insights into processes such as bread dough fermentation[48], bread baking[49], and freeze-drying kinetics[50]. Given the added flexibility in terms of experimental setups, these are attractive for investigating and uncovering theories related to the deep-frying process.

Here, we developed and applied time-resolved X-ray computed tomography in a synchrotron setting to visualise the deep-frying process under real-world conditions. An in-situ deep-frying setup was constructed and operated remotely with precise controls over sample positioning, oil frying temperature and deep-frying time during imaging. The 4D aspect of this study facilitated quantitative evaluation of the dynamics of oil uptake and spatial distribution inside WFD-based formulation during and after deep-frying. High-speed dynamic imaging optimised for both temporal and spatial resolution enabled the study of changes in the 3D porous microstructure, oil content and oil distribution in WFD deep-fried at different temperatures. Complimentary measurements monitoring the temperature and moisture content (MC) evolution of WFD are used to elucidate the microstructural changes observed by tomography. The knowledge gained through these experiments stands to enhance the understanding of oil uptake behaviour and pore morphology development throughout the deep-frying process and thereby, enhance the understanding of factors that impact the rapidly changing microstructural dynamics of foods undergoing this process[51]. The learnings open doors for future investigations on how product formulations or processing parameters can be tailored to manufacture deep-fried food products that align with consumer sensory expectations and health guidelines.

Results

4D μCT (three spatial dimensions and time) was performed to study the microstructural changes and oil uptake dynamics at various time points during 56 s of the deep-frying process and subsequent 63 s of the post-frying cooling of WFD samples (40% moisture content). Different deep-frying temperatures (180, 150 and 120 °C) were considered which resulted in distinct microstructural changes during deep-frying and thus enabled understanding the influence of process conditions on porosity development and consequent oil uptake dynamics. The moisture content was determined at various stages of the deep-frying process to evaluate how moisture loss dynamics at different deep-frying temperatures relate to the observed microstructural changes. Furthermore, local temperature profiles were measured beneath the surface (representing the crust regions) and at the centre (representing the core regions) during deep-frying and post-frying cooling to monitor the evolving temperature gradient, including the advancement of the evaporation front, and its effect on structure deformation.

High-speed dynamic imaging was carried out on the ID19 beamline at European Synchrotron Radiation Facility (ESRF, Grenoble, France) capable of ultrafast tomography at high spatial resolution[52,53]. To place results from the time-resolved investigation in context, the WFD samples were imaged before deep-frying using lab-based μCT (see "Methods"). Samples containing 50 mg dry matter (DM) were fitted into a sample holder to create images with a voxel size of 2.2 μm during deep-frying and 5.2 μm during subsequent ambient cooling. Figure 1a shows the scheme of a custom experimental setup equipped with remote vertical sample manipulation in a synchrotron tomography setting, with the actual setup

https://doi.org/10.1038/s41467-025-57934-z

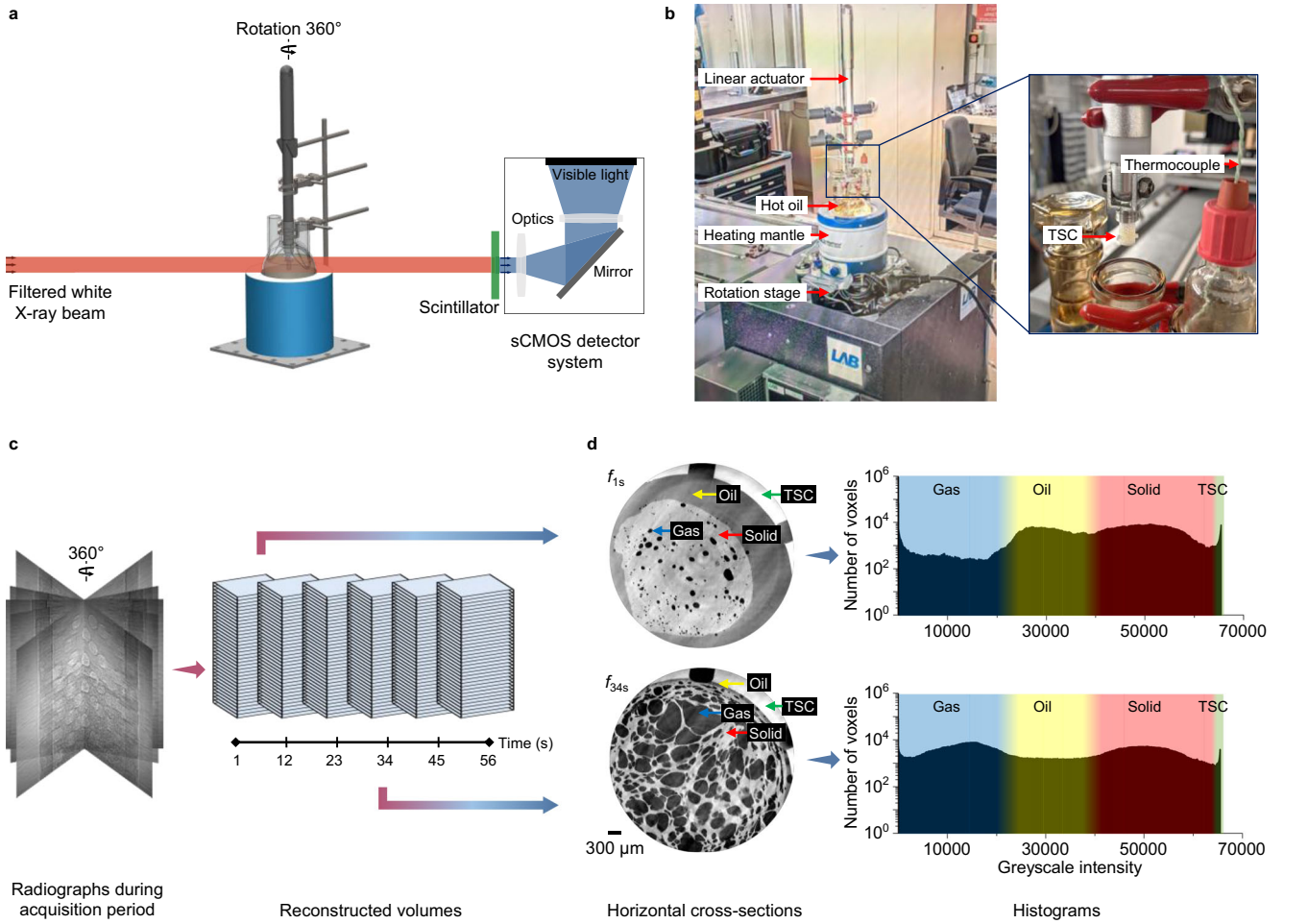

Fig. 1 | Schematic overview of the fast in-situ synchrotron x-ray tomography setup. a Experimental setup at the ID19 beamline of ESRF (Grenoble, France). A filtered white X-ray beam passes through the rotating sample while transmission radiographs are collected by a fast sCMOS indirect detector system; **b** Experimental setup mounted on the rotation stage for fast acquisition, (inset) the sample container is fixed to the linear actuator for remote sample manipulation during and after the deep-frying process; **c** Radiographs captured at six successive timepoints over the acquisition period, subsequent reconstructed volumes comprised of greyscale cross-section images; **d** Representative horizontal cross-sections from the reconstructed 3D volumes (at time points 1 s and 34 s during deep-frying) with different phases annotated based on the intensity value, corresponding segmentation on the greyscale intensity histogram with intensity ranges marked in distinct colours for identification of phases, solid (red), oil (yellow), gas (blue), TSC (green), influenced by their attenuation characteristics.

pictured in Fig. 1b (for detailed description of setup operation and acquisition protocol, see "Methods"). Using filtered back propagation reconstruction with phase retrieval (Fig. 1c), 3D volume images were obtained that render the porous microstructure contrasting the solid matrix, gas or oil filled pores and frying oil in addition to the Teflon sample container (TSC) (Fig. 1d). Here, the highly attenuating solid phase (representing the deep-fried WFD) appears brighter in the tomograms, thus enabling the separation from the lowly attenuating gas, whereas the oil phase lies in-between these two phases due to differences in X-ray attenuation and phase effects. The phases were not differentiated based solely on their greyscale intensity thresholds, but together with spatial and temporal context at different stages during acquisition. As the sample expanded during deep-frying, the space it occupied increased due to increasing gas volume (representing increased histogram fraction) thus displacing the oil volume (representing a decreasing histogram fraction).

Rapid pore expansion during deep-frying deforms structure

The µCT images of the WFD samples before deep-frying revealed the dough material phase with uniformly distributed gas-filled pores (Fig. 2a), more commonly termed as gas cells in cereal research[54]. Gas pores occupied 4.2% ± 0.1% of the volume with ca. 15 µm mean pore size diameter, ranging from 5 to 178 µm (pore size distribution shown in Supplementary Fig. 1).

Horizontal cross sections of WFD samples undergoing structural change during deep-frying at 180 °C are presented in Fig. 2b, the accompanying Fig. 3 shows the corresponding vertical cross-sections. Upon initial contact of the WFD sample with the frying oil (i.e., 1 s after immersion), the dense microstructure consisting of numerous, small gas-filled pores was still visible and resembled the structure of the non-fried WFD sample. At this stage of deep-frying, convective heat transfer from the hot frying oil merely results in superficial boiling, initiating the instantaneous conversion of water to vapour and formation of steam bubbles at the surface[11].

Through continued heat conduction inside the sample, the temperatures below the surface rapidly approached the boiling point of water, while heat conduction progressed more slowly into the centre (Fig. 4b). As a consequence of the increased steam generation and rising gas pressures, deformation was initiated by expansion of pre-existing pores, essentially serving as nucleation sites. The structure expanded during the early stages of deep-frying (i.e., between 1 and 13 s) and was transformed into a highly porous solid matrix (Fig. 3a). Parts of the starch-gluten network were observed to rupture under

https://doi.org/10.1038/s41467-025-57934-z

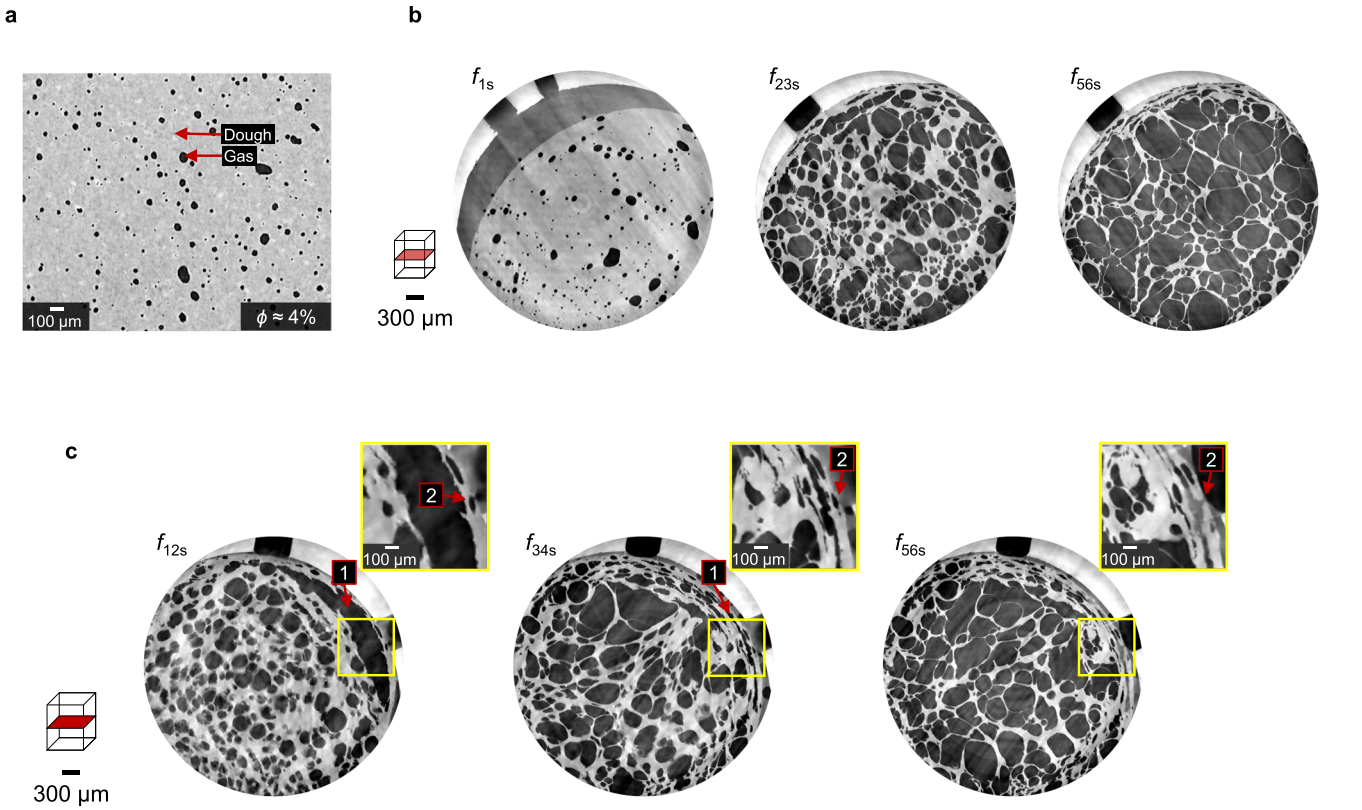

Fig. 2 | Microstructure development in WFD samples during deep-frying at 180 °C. a Reconstructed slice of the WFD sample before deep-frying exhibiting a homogeneous structure incorporating uniformly distributed gas-filled pores; **b** Reconstructed slices of the changing microstructure over the course of deep-frying; **c** Regions of interest (yellow squares) in the X-ray CT slices at different deep-frying times: (1) formation of large pores at the edge of samples subsequently compressed under internal expansion of pores, (2) localised oil ingress through ruptured walls of open pores at the surface during late stages of deep-frying. Scale bars indicated in µm; time labels f_i denote observations during deep-frying period, subscripts denote the time in seconds.

continued expansion, thus forming large pores as smaller adjacent gas pores coalesced. At this stage, the moisture content was ≈0.544 g g^{-1} DM ($MC_{180°C,15s}$, Fig. 4a) indicating that the sample had lost a small portion of water. Moisture was primarily removed through vaporisation at the surface, where it was convected away by the oil[23]. Internally, as vapour pressure increased due to evaporation at pore-matrix interfaces throughout the material, moisture gradually diffused from regions of higher saturation towards the surface[11,55]. This thus substantiates that persistent volumetric expansion induced by water evaporation and consequent enlargement of steam-filled pores inside the WFD solid structure increasingly exerted more forces on the internal walls resulting in thinning of the solid matrix.

Between 19 and 23 s, the temperatures in the crust plateaued at around 100 °C for a brief period before increasing at a slower rate thereafter (Fig. 4b). This brief period where temperatures in the crust plateaued suggests that the evaporation front advanced to the core regions once sufficient moisture was removed from the crust. Expansion in the core regions continued as temperatures level to 100 °C (Fig. 4b), simultaneously pushing the surface layers against the inner walls of the sample holder (observed from 23 s onwards in Figs. 3b and 2c) indicated a high flexibility of the biopolymer constituents hampering vapour escape at the surface during the early stages of deep-frying[11,56].

Temperatures steadily increased above 100 °C in the crust, while stabilising around the boiling point of water in the core (Fig. 4b). Prolonged moisture loss ($MC_{180°C,30s} \approx 0.356$ g g^{-1} DM, Fig. 4a) prompted the formation of a distinct region representing a crust-like structure after 34 s of deep-frying (Fig. 2c). Moisture migration from the core to the crust continued through a combination of pressure-driven convection and capillary diffusion for both vapour and liquid water[11,57], while moisture was continually removed from the crust through diffusion and convection of vapour. Crust formation was facilitated by the slower moisture migration from the core compared to the rapid vaporisation at the surface[23]. The crust was largely composed of numerous small, flattened pores with thick walls, while the core region consisted of larger irregular pores with thin walls. Expansion inside the highly porous structure successively slowed down between 45 and 56 s of deep-frying, which was attributed (in part) to the substantial loss of moisture (final $MC_{180°C,60s} \approx 0.167$ g g^{-1} DM, Fig. 4a) and the increased structural rigidity of the biopolymers in the WFD system[33]. The majority of internal heat flow was directed towards converting liquid water to vapour by boiling observed by the continued core temperature plateau at 100 °C. Studies on the microstructure of potato-based products have attributed the formation of small pores in the crust to sample shrinkage induced by moisture loss after prolonged deep-frying[25]. However, dynamic imaging of the deep-fried WFD system here shows that these small pores are formed due to the expansion of the core regions and the subsequent compression of pores below the surface.

Starch and gluten in the samples progressively undergo structural transformations during deep-frying[58]. In the WFD system, despite starch being a major component, the structure is primarily supported by the viscoelastic gluten network due to the extensive structural changes that occur during deep-frying[33,59]. However, it was recently shown that the transition of potato starch (in potato starch-water model systems) from the rubbery state, after gelatinisation, to the glassy state, is necessary to maintain the expanded structure due to frying-induced water evaporation[14]. Changes in the moisture content of the sample at different stages of deep-frying, together with temperature measurements in the crust and core, provides additional

https://doi.org/10.1038/s41467-025-57934-z

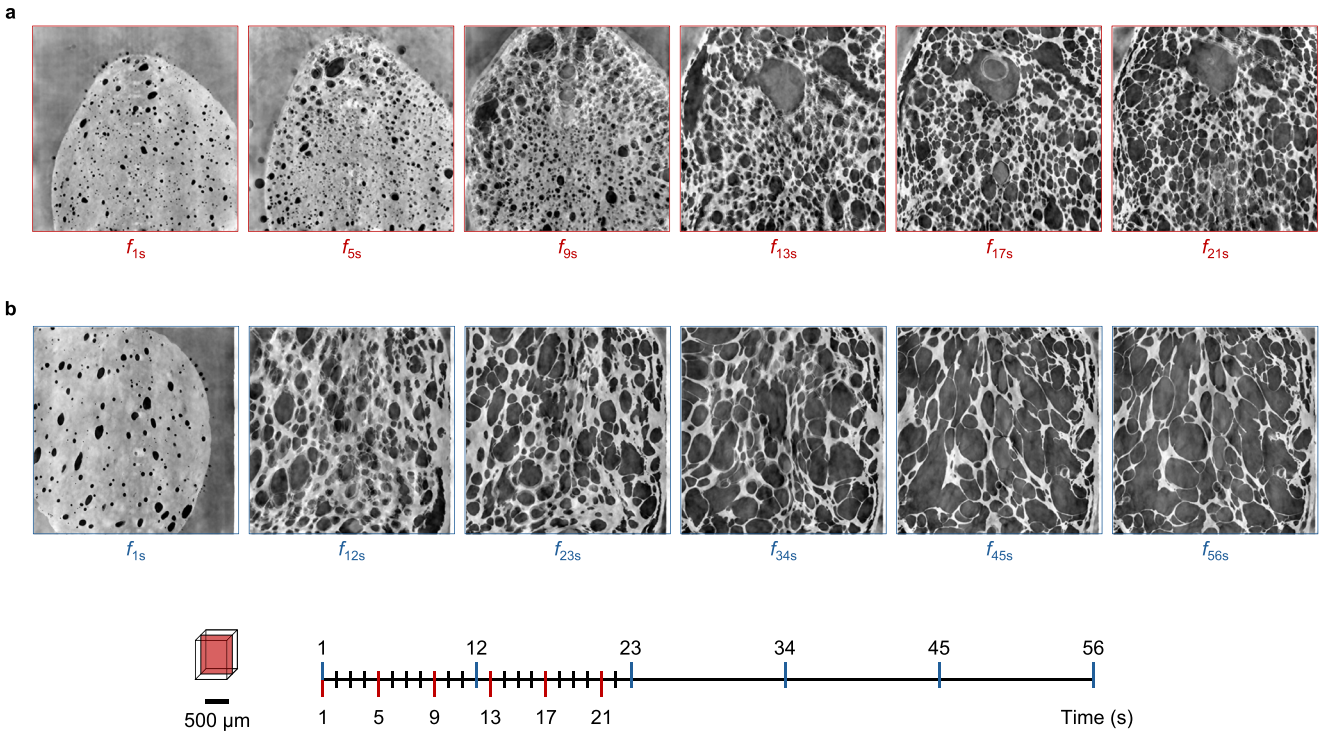

Fig. 3 | Vertical cross-sections of reconstructed images highlighting microstructure development in WFD samples during in-situ deep-frying at 180 °C. **a** Reconstructed images follow the expansion of WFD structure during the first 21 s (observations every 4 s) after immersion in hot oil; **b** Reconstructed images follow the development of WFD microstructure during 56 s of deep-frying (observations every 11 s). Scale bar indicated in µm; time labels f_i denote observations during deep-frying period, subscripts denote the time in seconds.

insights into the conditions underlying structural transitions inside the WFD system. Through heating, the temperature increased to the boiling point and water evaporated. Temperatures in the crust increased from 100 °C (25 s) and reached ≈135 °C by the end of deep-frying. Continued loss of moisture and increasing temperatures below the surface led to a rigid crust after transitioning into a glassy state[29,33]. In the core, temperatures stabilised at 100 °C with steam trapped inside the structure, suggesting that the amount of moisture in this region was sufficient for the biopolymers to remain in a rubbery state, thereby supporting structure expansion induced by steam generation. Image data depicting structure expansion during deep-frying reveals minimal structure alteration of hardened surface regions while the central regions continually deform (Fig. 3), indicating a difference between the physical states of crust and core regions at the end of 56 s of deep-frying.

The pressure exerted by escaping gases from continuous vapour generation during deep-frying inhibits oil entry into the structure[4,22,31]. In addition, the absence of suitable pathways from the crust to core regions also significantly impeded oil uptake below the surface even after extensive structural deformation during deep-frying. Pores present in the outer crust regions were distinctly disconnected to the core regions of the sample, as seen from the labelled pore space in Supplementary Fig. 2. Even when oil was detected in pores near the surface, it was unable to penetrate further into the sample indicating lack of connectivity to other adjacent pores as seen compressing during internal expansion (Fig. 2c). This oil ingress likely corresponds to so-called 'structural oil' entering the food matrix during deep-frying[15,30].

Post-frying oil uptake

Extensive structure deformation during deep-frying and the microstructural characteristics at the end of the process serve as the basis for understanding the mechanisms by which oil uptake occurs during the cooling phase immediately after deep-frying. Here, the 3D images captured post-frying were segmented with the help of machine learning assisted pixel classification in Ilastik v1.4.0[60] (Fig. 5 shows the image processing workflow, for detailed description see "Methods"). The aim of segmentation was to quantify the amount and location of oil in the porous structure as well as to analyse the connectivity of pores across the fried sample volume. The classifier accounted for the uncertainty in assigning labels (as seen from the uncertainty map in Fig. 5)[60], which was considered as an additional uncertainty range in the calculated segmented volumes of the different phases (see "Methods"). Through segmentation, the different phases (oil, gas, and solid matrix) were separated and quantified (volume fractions and porosity presented in Table 1). Furthermore, volumetric renderings of the samples deep-fried at 180 °C (Fig. 6a) provide a spatial representation of the changes in oil distribution during cooling. The morphological properties of the crust (considered as a 0.5 mm thickness subsurface layer) and core (remaining internal regions) were evaluated by using the local structure thickness of the solid gas cell walls (presented in Supplementary Fig. 6 and Supplementary Table 1) and pore size distributions (Supplementary Fig. 7a).

After removing the samples from the frying oil, the internal temperatures began to drop. The rate of temperature decrease varied significantly between the crust and core, with the crust cooling faster than the core (Fig. 4b). It is of note that the core temperatures did not fall below 100 °C during the post-frying cooling phase assessed here (i.e., 63 s), as the crust insulated the core regions. After 8 s of cooling, the WFD sample displayed a highly porous, thin-walled microstructure that resembled the structure at the final time point of deep-frying. The structure presented ca. 4.5% of the characterised volume as the oil fraction and exhibited a gas porosity of ca. 44.2%. As shown in Fig. 6a, oil content increased during the cooling period as surface oil and oil available in the sample holder was gradually pulled into the structure (rising to ca. 14.4% ± 1.3% after 63 s, see Supplementary Fig. 3). No noteworthy structure deformation was observed throughout the

https://doi.org/10.1038/s41467-025-57934-z

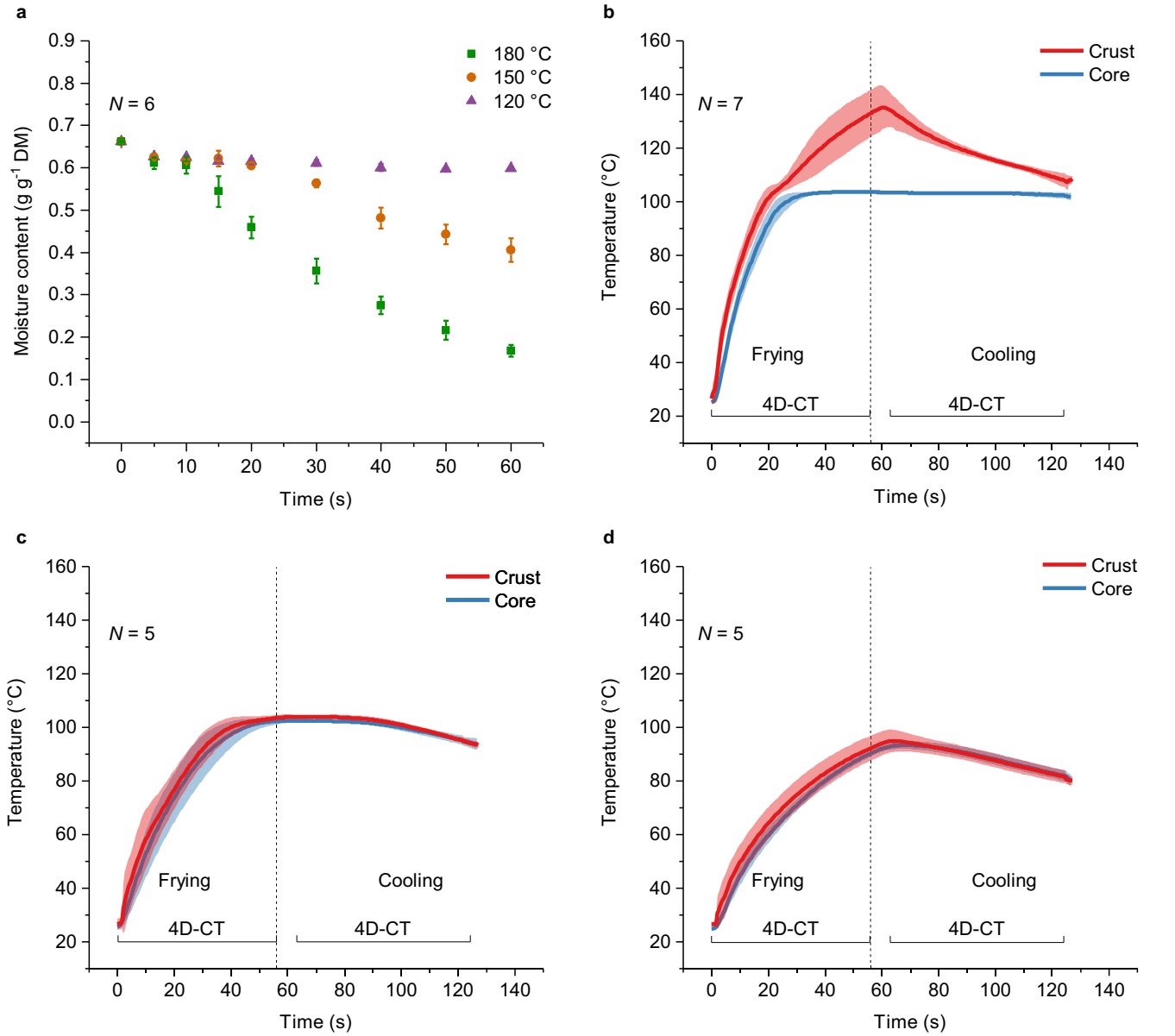

Fig. 4 | Moisture content and temperature measurements of WFD samples. **a** Moisture content of non-fried (0 s) and deep-fried (5 – 60 s) WFD samples with initial hydration levels of 40% deep-fried at different temperatures (180 °C in green, 150 °C in orange and 120 °C in purple). MC is calculated on an oil free dry matter basis [m_{H2O} ($m_{dough\ DM}$)$^{-1}$], where mass (m) is expressed in grams and DM is the dry matter of the dough in grams. Means are calculated over six measurements, error bars represent standard deviations; Local temperature measurements inside the WFD samples during deep-frying and post-frying cooling at different oil temperatures (**b** – 180 °C, **c** – 150 °C, and **d** – 120 °C). The temperature measurements correspond to the deep-frying and post-frying cooling phases, separated by a vertical dotted line, and aligned with periods of 4D µCT observations. Each plot presents mean temperature profiles in the crust and core regions inside the samples, shaded regions represent the standard deviation across five or seven measurements.

cooling period (gas porosity in Table 1), confirming that the solid matrix formed during deep-frying was sufficiently rigid to resist any significant structural collapse. It has been reported that, as temperatures drop, gas expulsion from the surface stops due to negative gauge pressures induced by condensing vapours[12,61], which subsequently pulls oil into open pores at the surface. However, in the WFD samples the temperatures stayed above 100 °C in both the crust and core regions at the end of 63 s during cooling. Although the oil uptake associated with the vacuum effect from condensing vapours cannot be completely ruled out, it is more likely that the observed oil uptake was primarily driven by capillary action in the small crust pores, as the vapour pressures inside these pores could not drop below the atmospheric pressure. In tortilla chips, oil content was also found to be primarily influenced by small pores exerting great capillary action before condensation occurs[26]. The crust comprising of mostly small, connected pores (pore size distribution shown in Supplementary Fig. 7a) was saturated with oil[25].

Pore connectivity

The 3D volume renderings during cooling show most of the oil concentrated in pores below the surface, with small amounts of oil detected in the core having high prediction uncertainty during segmentation (Fig. 6a). Labelling the segmented images provided a means to indicate connectivity of pore volumes and revealed that pore-filling progressed gradually through discrete sub-networks of connected pores (Fig. 7a). These findings also confirmed that oil uptake was mainly limited to the outer crust region of the sample (see Supplementary Fig. 3). During deep-frying the pore-space

https://doi.org/10.1038/s41467-025-57934-z

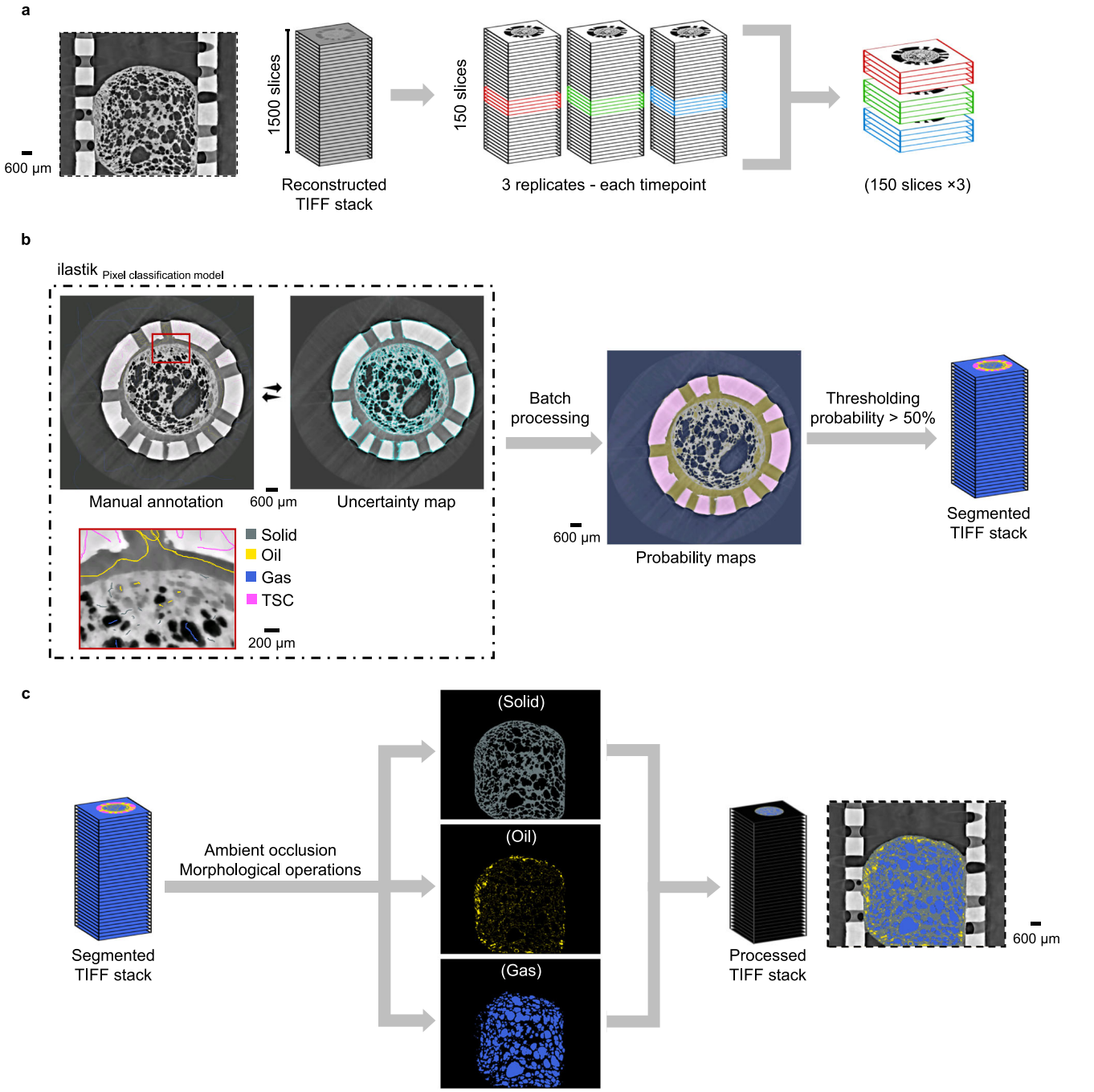

Fig. 5 | Image processing workflow for the post-frying cooling X-ray CT dataset. **a** 10% of the greyscale cross-sectional images from the reconstructed volumes of each replicate were imported into ilastik using the ilastik4ij plugin (https://github.com/ilastik/ilastik4ij) in Fiji. **b** A pixel classification model was trained iteratively for different timesteps by manually annotating the different phases: deep-fried solid WFD (grey), oil (yellow), gas (blue), and TSC (pink), while minimising uncertainty in class predictions. Probability maps for the phases were generated for the complete volumes and subsequently segmented using a thresholding probability > 50% to obtain the segmented image stack. **c** Ambient occlusion and other morphological operations were applied on the segmented images to isolate the sample boundaries and separate the individual phases for quantification. Scale bar indicated in µm.

continually expanded in the core region and compressed pores in the outer regions of the structure, resulting in a higher frequency of smaller pores in the crust (see Supplementary Fig. 7a). The minimal pore connectivity between the crust and the core due to an intact wall network prevented large amounts of oil from penetrating deeper into the structure, with most of the oil identified in small, compressed pores near the surface. Perhaps the most important finding with an implication for oil uptake is that the connectivity of the pore network below the crust was altered due to the continued internal expansion during deep-frying (as seen in Supplementary Fig. 2).

Microstructure and oil uptake influenced by oil temperature

Figure 8 shows the microstructure development of the samples during deep-frying at 120 °C (Fig. 8a) and 150 °C (Fig. 8b). Similar to what had been shown when deep-frying at 180 °C, structure expansion initiated from the pre-existing gas cells present in the non-fried dough. However, gas cell sizes increased at a notably slower rate in these samples

https://doi.org/10.1038/s41467-025-57934-z

Table 1 | Oil content and porosity of fried wheat flour dough (WFD) formulation with 40% moisture content evaluated during post-frying cooling

Oil temperature	Cooling time (s)	Volume fraction of oil (% oil/sample volume)	Volume fraction of oil (% oil/solid)	Gas porosity (%)	Total porosity (%)
180 °C	8	4.47 (2.72)^{cd}	7.90 (4.67)^{d}	44.20 (1.90)^{a}	48.67 (1.77)^{ab}
	19	4.32 (1.65)^{cd}	7.76 (2.79)^{de}	45.01 (2.18)^{a}	49.33 (0.79)^{ab}
	30	9.28 (0.75)^{b}	16.39 (1.05)^{bc}	43.43 (1.55)^{a}	52.71 (1.11)^{a}
	41	8.55 (0.08)^{b}	14.97 (0.40)^{c}	42.87 (1.12)^{a}	51.42 (1.18)^{a}
	52	12.33 (0.40)^{ab}	22.30 (0.78)^{ab}	44.68 (1.23)^{a}	57.02 (1.21)^{a}
	63	14.42 (1.34)^{a}	24.04 (1.76)^{a}	40.09 (1.25)^{ab}	54.51 (0.17)^{a}
150 °C	8	8.12 (1.13)$^{\dagger bc}$	11.66 (1.82)$^{\dagger cd}$	30.16 (1.22)$^{\dagger bc}$	38.28 (2.35)$^{\dagger bc}$
	19	10.66 (0.79)$^{\dagger ab}$	14.70 (1.72)$^{\dagger cd}$	27.09 (3.15)$^{\dagger cd}$	37.75 (3.94)$^{\dagger bc}$
	30	10.73 (1.12)^{ab}	13.06 (1.87)^{cd}	17.40 (3.37)^{def}	28.12 (4.43)^{cd}
	41	11.88 (1.02)^{ab}	13.87 (0.30)^{cd}	14.42 (5.94)^{ef}	26.30 (4.95)^{cd}
	52	12.22 (0.43)^{ab}	14.24 (0.63)^{c}	13.97 (5.39)^{ef}	26.20 (5.09)^{cd}
	63	12.20 (0.90)^{ab}	14.29 (1.31)^{c}	14.36 (4.60)^{ef}	26.56 (4.75)^{cd}
120 °C	8	1.15 (0.34)^{d}	1.53 (0.51)^{ef}	24.13 (3.71)^{cde}	25.28 (3.93)^{de}
	19	1.08 (0.34)^{d}	1.30 (0.41)^{f}	17.29 (2.36)^{def}	18.36 (2.37)^{def}
	30	1.09 (0.45)^{d}	1.25 (0.51)^{f}	13.35 (1.74)^{ef}	14.44 (1.51)^{ef}
	41	1.18 (0.57)^{d}	1.32 (0.62)^{f}	11.39 (1.65)^{f}	12.58 (1.21)^{f}
	52	1.29 (0.65)^{d}	1.43 (0.70)^{f}	10.68 (1.48)^{f}	11.96 (0.96)^{f}
	63	1.28 (0.71)^{d}	1.41 (0.76)^{f}	10.21 (1.48)^{f}	11.49 (0.84)^{f}

Values represent the mean ($N = 3$, $^{\dagger}N = 2$) with standard deviation presented in brackets. Values in the same column are significantly different ($p < 0.05$) when not sharing the same lower-case alphabetic character.

compared to those deep-fried at 180 °C (see Supplementary Fig. 4). This delayed expansion is attributed to the slower steam formation at lower deep-frying temperatures since heat conduction inside these samples progressed at a slower rate. Internal thinning of the solid matrix continued from sustained expansion in the core regions. Temperatures within the samples did not exceed 95 °C (Fig. 4d) and 100 °C (Fig. 4c) when deep-fried at 120 °C and 150 °C, respectively. The more uniform temperature distribution observed in these samples, compared to those deep-fried at 180 °C, resulted from coupled heat and mass transfer mechanisms in the deforming structure. Slower heating occurred due to lower convective heat transfer coefficients at the surface, leading to lower vapour pressures, reduced surface water loss, and incomplete liquid water evaporation[11,62]. Consequently, the temperatures did not rise above the boiling point during deep-frying, allowing for a more uniform temperature distribution within the sample. In contrast, deep-frying at 180 °C resulted in significant temperature gradients between the crust and the core, driven by higher heat flux, increased vapour pressures, and rapid vaporisation at the surface[23].

Comparing the microstructures of deep-fried (56 s) WFD samples at 180 °C and 120 °C, those deep-fried at 120 °C presented a more uniform pore morphology without a distinct crust (see Supplementary Fig. 4a). As the internal temperatures of samples deep-fried at 120 °C did not reach the boiling point of water, the structure did not show signs of extensive deformation including thin wall rupture (Supplementary Fig. 4a). The higher residual moisture content after deep-frying (final $MC_{120°C,60s} \approx 0.599\ g\ g^{-1}$ DM, Fig. 4a) suggests that most internal regions still existed in a rubbery state, preventing any apparent rupture of the thin-walled structures in the core. Moisture loss occurred at the surface through low equilibrium vapour pressures and low convective heat transfer coefficients[62]. The smaller temperature difference between the surface and the core regions indicates negligible water vapour gradients, suggesting that internal moisture migration was slow and driven by diffusion[23]. On the other hand, the microstructure in WFD samples deep-fried for 56 s at 150 °C revealed a structure with larger, irregular pores formed due to the rupturing thin walls of the solid matrix and more advanced gas cell coalescence (see Supplementary Fig. 4b). A distinct, thick crust was observed in Fig. 8b with small, flattened pores analogous to the crust microstructure of WFD deep-fried at 180 °C (Fig. 2b). Heat flow was faster than at 120 °C but slower than at 180 °C. The slower increase in surface temperatures during deep-frying at 150 °C reduced the overall moisture loss from the crust compared to deep-frying at 180 °C. This resulted in higher residual liquid water content throughout the process (final $MC_{150°C,60s} \approx 0.405\ g\ g^{-1}$ DM Fig. 4a), as evidenced by the temperature plateau around the boiling point of water in both the crust and core (Fig. 4c).

No significant oil ingress was observed during deep-frying in samples deep-fried at low temperatures (see Supplementary Fig. 4). Oil temperature significantly affected the moisture loss kinetics in WFD samples due to differences in the rate of heat conduction (Fig. 4). Gradual internal structure expansion was observed at temperatures approaching the boiling point of water, as a result of slow vapour generation. Similar microstructural features were seen among samples deep-fried at 180 °C after 12 s (Fig. 3b), 150 °C after 23 s (Supplementary Fig. 4b) and 120 °C after 34 s (Supplementary Fig. 4a) with moisture content measuring at $\approx 0.606\ g\ g^{-1}$ DM in all samples (Fig. 4a). At temperatures around 100 °C, more violent structure deformations such as formation of large pores and thin wall rupture were induced by continuous evaporation and increasing vapour pressure inside the structure. This was apparent from the reconstructed images for samples deep-fried at 180 °C after 23 s (Fig. 3b) and at 150 °C after 45 s (Supplementary Fig. 4b), which corresponded to similar moisture content values of $0.459\ g\ g^{-1}$ DM ($MC_{180°C,20s}$) for 180 °C and $0.443\ g\ g^{-1}$ DM ($MC_{150°C,50s}$) for 150 °C (Fig. 4a). The slower rate of moisture loss in samples deep-fried at 150 °C, compared to those at 180 °C, can be attributed to the lower convective heat transfer coefficients and lower equilibrium vapour pressures[62].

After removal from the hot oil (i.e., 8 s of cooling), the WFD samples deep-fried at 120 °C and 150 °C preserved their porous microstructures (Fig. 6), thus resembling the structures observed at the final time point of deep-frying (Fig. 8). However, these samples progressively collapsed during the cooling period, shrinking to less than half of their initial gas porosity (Table 1) as the internal core

https://doi.org/10.1038/s41467-025-57934-z

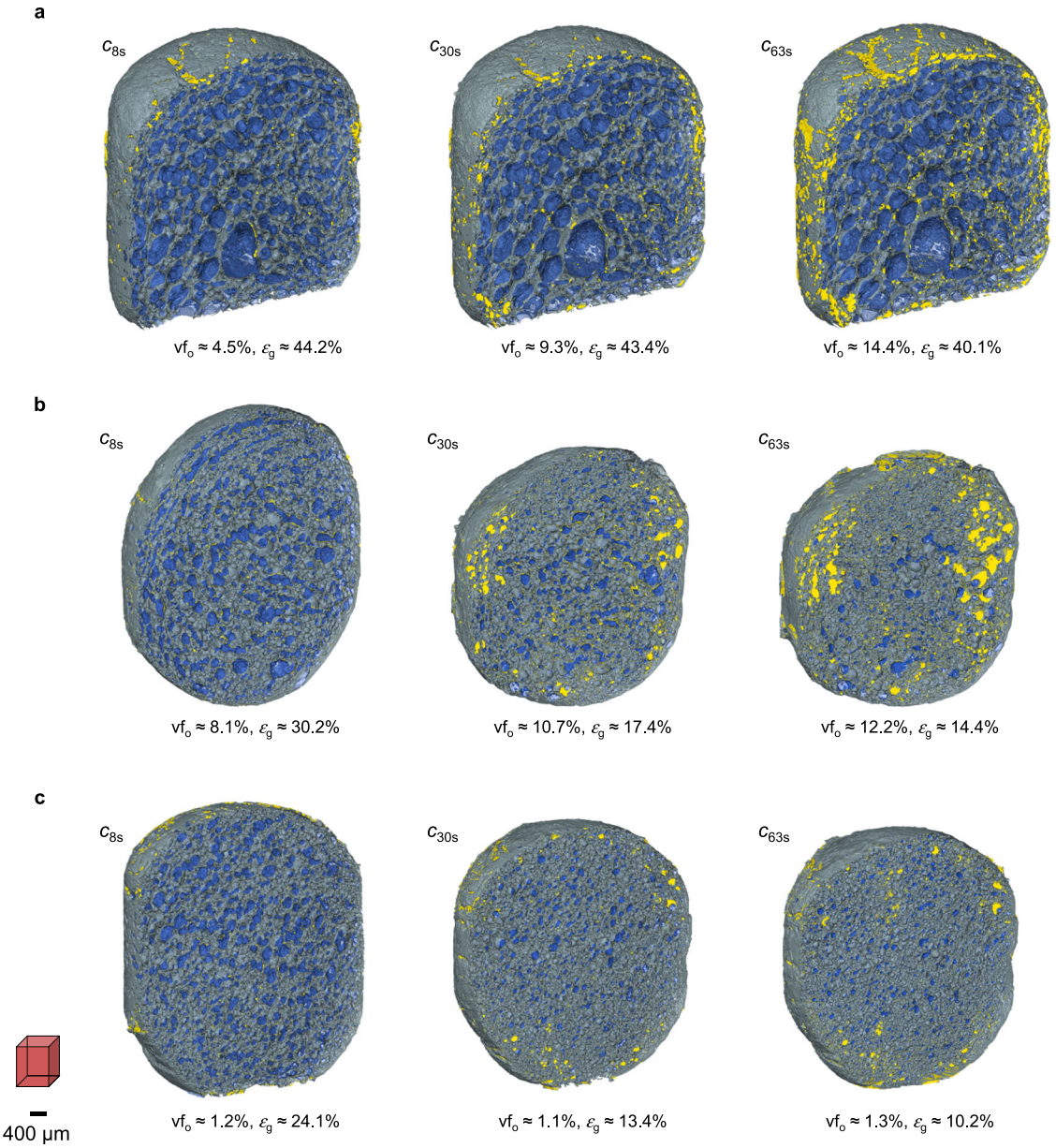

Fig. 6 | 3D volume renders of WFD samples during the post-frying cooling period. Rows correspond to WFD samples deep-fried at different temperatures (**a** – 180 °C, **b** – 150 °C and **c** – 120 °C). **a** Oil was observed invading the small pores in the distinct crust region of the sample. Internal segmented oil spots are associated with high uncertainty levels; **b** Samples fried at 150 °C. Here, the structure collapse was accompanied by oil content rising with decreasing gas porosity; **c** Samples fried at 120 °C. The structure collapsed over the observed duration, but the oil content stayed relatively constant with decreasing gas porosity. Scale bar indicated in µm; segmented phases depicted as deep-fried solid WFD (grey), oil (yellow), and gas (blue); time labels c_j denote observations during cooling after retraction from oil, subscripts denote the time in seconds after retraction from oil; vf_o denotes volume fraction of oil; ε_g denotes gas porosity.

collapsed (see Supplementary Fig. 5 and Supplementary Table 1). This phenomenon was likely related to the sustained rubbery state of biopolymers due to higher residual moisture (final $MC_{120°C,60s} \approx 0.599\ g\ g^{-1}$ DM, $MC_{150°C,60s} \approx 0.405\ g\ g^{-1}$ DM Fig. 4a) resulting from steam accumulation inside the core regions of the structures during deep-frying. Core regions lacking sufficient rigidity were unable to maintain the expanded shape as steam condensation induces negative vapour pressures due to reducing temperatures during cooling[2,11,63].

Analysis of the morphology in the separated crust and core regions in comparison to WFD samples deep-fried at 180 °C reveals significant differences ($p < 0.05$) in the structure collapse behaviour of WFD samples deep-fried at 120 °C and 150 °C (Supplementary Table 1). The frequency of smaller pores (0 – 50 µm) increased significantly after collapse in both crust and core regions (Supplementary Fig. 7b, c). In samples deep-fried at 120 °C, the distributions of local cell wall thickness in the 'crust' and 'core' regions were virtually indistinguishable (Supplementary Fig. 6). The average structure thickness in the evaluated 'crust' regions was significantly different ($p < 0.05$) compared to the crust regions of the samples deep-fried at 150 °C and 180 °C (Supplementary Table 1), further supporting the observation that no distinct crust was formed in these samples during deep-frying. In contrast, in the samples deep-fried at 150 °C, the average structure thickness of the crust at 8 s was not significantly different ($p > 0.05$) from the crust in samples deep-fried at 180 °C at 8 s (Supplementary Table 1), confirming the presence of a rigid crust. Furthermore, during collapse, the shift in the distribution of local structure thickness towards thicker pore walls was notably slower in the crust than in the core, indicating that portions of the crust were more rigid than the core regions.

https://doi.org/10.1038/s41467-025-57934-z

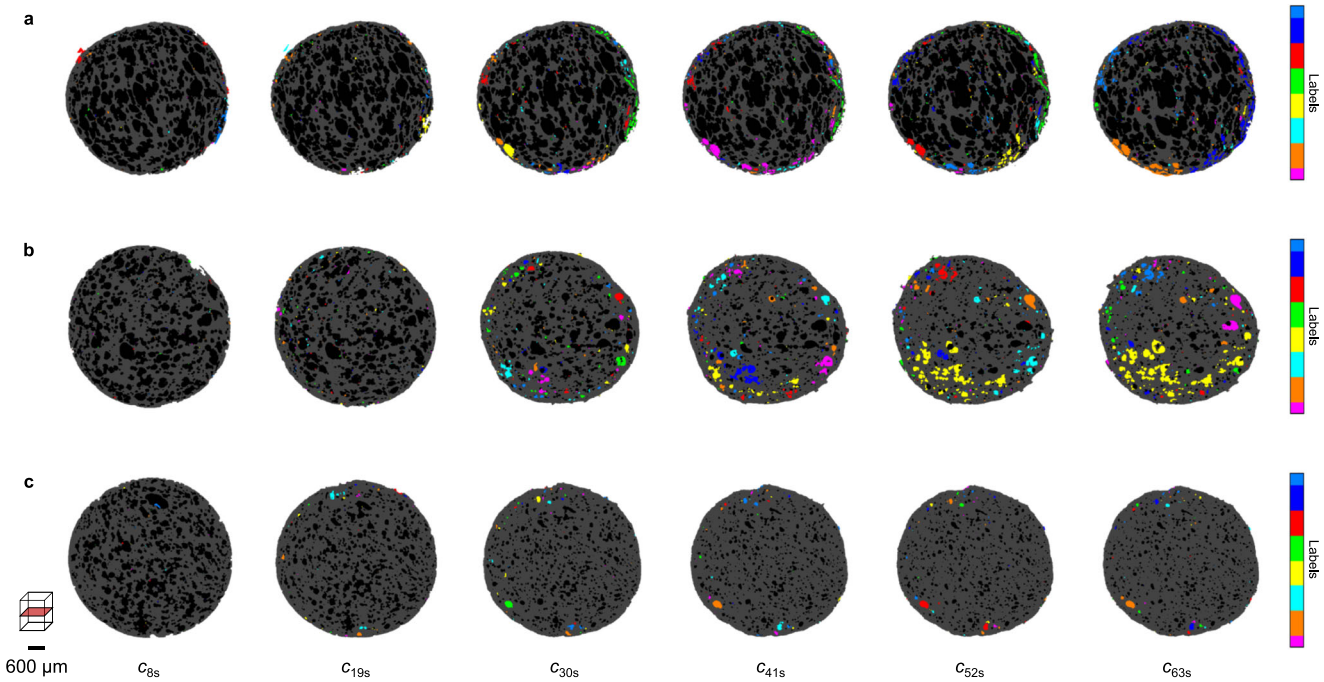

Fig. 7 | Horizontal cross-sections images of segmented and labelled oil-phase from in-situ X-ray CT during post-frying cooling. Rows correspond to WFD samples (depicted in grey) deep-fried at different temperatures (**a** – 180 °C, **b** – 150 °C and **c** – 120 °C). The segmented pores are labelled using a repeating categorical colormap where the same label colour of adjacent objects represents depicts a connected oil phase. The progression over time provides an overview of oil entering the internal regions of the sample through connected pores. Scale bar indicated in µm; time labels c_j denote observations during cooling after retraction from oil, subscripts denote the time in seconds.

Similar to the samples deep-fried at 180 °C, most of the oil absorption in samples deep-fried at lower temperatures occurred during cooling. Changing capillary pressures in crust pores and vapour condensation from temperatures decreasing below 100 °C inside the sample during cooling are both expected to have contributed to oil uptake. The samples deep-fried at 120 °C experienced significantly lower ($p < 0.05$) oil uptake across all samples due to the limited interconnectivity of pores at the surface due to lack of a distinct crust formation during deep-frying (Fig. 7c). Extensive structure collapse led to shrinking of pores inside the sample and collectively hindered oil ingress during cooling (Table 1 and Supplementary Fig. 7). In contrast, samples deep-fried at 150 °C displayed oil penetration in pores further below the crust during cooling (Fig. 7b). As the structure collapsed, pore connectivity between the crust and core was disrupted. The presence of a rigid crust led to the formation of surface-connected pores that extended deeper into the sample, allowing greater amounts of oil to enter below the crust (Fig. 6b).

Discussion

Despite growing health consciousness among consumers, deep-fried foods remain popular in the global snack market. Their high caloric density, resulting from oil uptake during the deep-frying process, has significant implications for both consumers with preferences for low-fat products and formulation strategies within the food industry. Innovations in healthier frying techniques and the formulation of new deep-fried products with reduced fat content require fundamental knowledge of the mechanisms governing oil absorption dynamics. However, the mechanisms resulting in deep-frying-induced oil uptake have been difficult to substantiate (much less visualise) due to the highly complex and intense nature of the process[2].

We demonstrated that high speed time-resolved X-ray tomography can be a useful technique for dynamic in-situ visualization of the deep-frying process and presented a comprehensive study exploring the spatial (in three dimensions) and temporal changes in microstructure during and after deep-frying and its impact on oil absorption dynamics. The effect of different frying temperatures was used to study differences in the structure deformation, oil uptake, and the development of crust and core regions in a model wheat flour dough (WFD) system.

The current study addresses the limitations of previously used imaging methods in this research domain (e.g., CLSM, SEM) that lack the combined spatial and temporal resolution necessary to capture this highly dynamic process. Using a bespoke, compact experimental setup with adjustable temperature control and remote operation in a synchrotron setting, we eliminated the need for sample manipulation during and after deep-frying. Additionally, optimised spatial and temporal resolutions enabled fast acquisition at 1 tomograph per second, allowing us to resolve critical features of the evolving internal microstructure and capture previously unobservable events, such as the influence of pore connectivity on oil uptake. This technique facilitates relatively easy adjustments to the acquisition protocol in terms of frying conditions (duration, temperature), spatial and temporal resolution, allowing for the investigation of specific phenomena related to the deep-frying process.

Despite the clear advantages offered by the presented technique, certain limitations remain. First, the water phase was not resolved in the images and was lumped together with the solid matrix due to complex interactions between the sample constituents, which made it challenging to validate established moisture loss mechanisms[11,55]. However, ongoing improvements in state-of-the-art instrumentation at neutron sources are generating interest in the combined use of fast neutron and X-ray imaging[64]. The higher neutron sensitivity of hydrogen atoms holds great potential for visualising moisture transport in deforming media, such as during deep-frying[65].

Second, motion artefacts hindered phase segmentation of images captured during deep-frying. Balancing the spatial and temporal resolution, alongside data processing demands remains a key challenge. However, innovations in rotation free X-ray multi-

https://doi.org/10.1038/s41467-025-57934-z

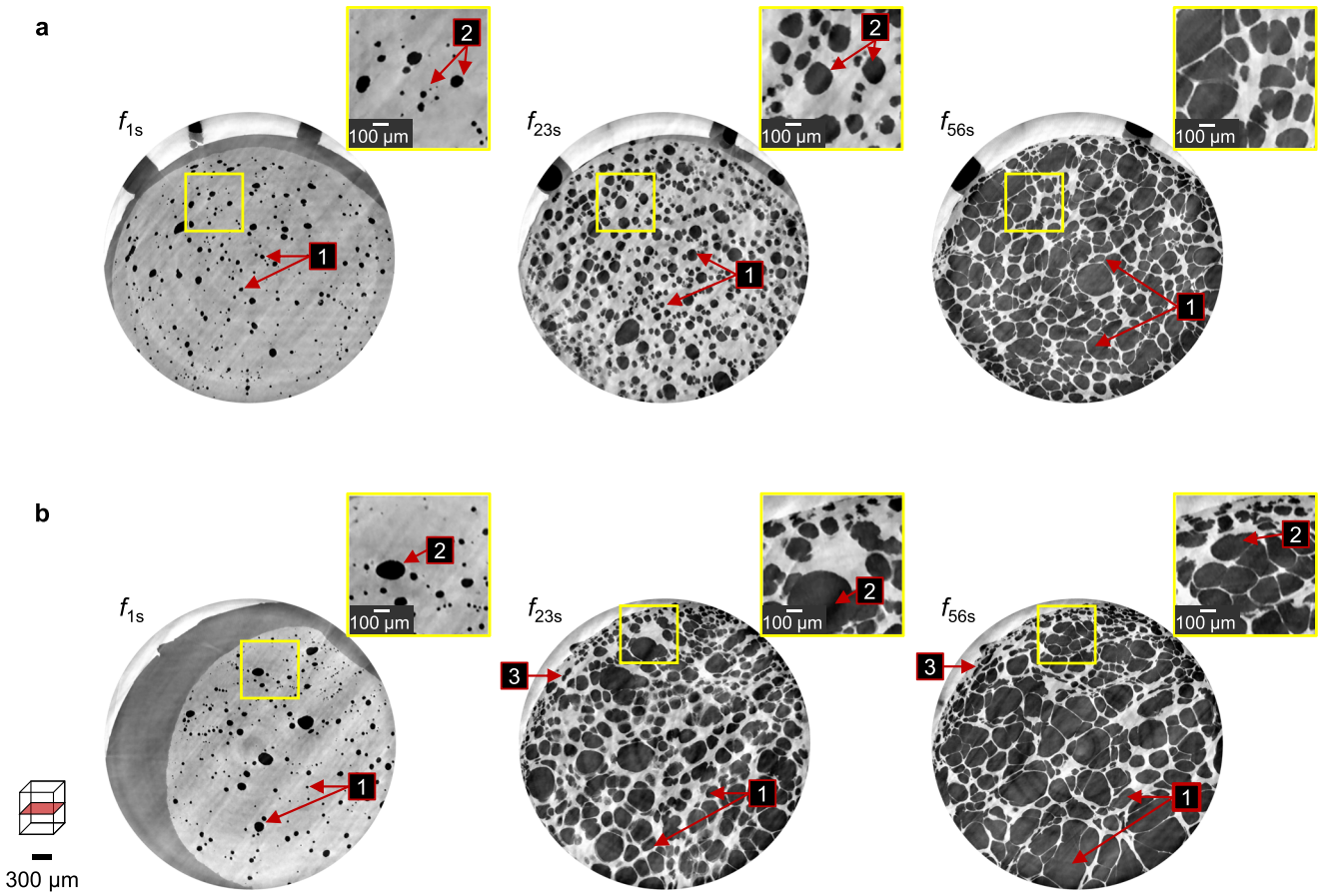

Fig. 8 | Microstructure development in WFD samples during deep-frying at 120 °C and 150 °C. a Regions of interest (yellow squares) in the X-ray CT slices of samples fried at 120 °C: (1) Transformation of the dense sample into a highly porous microstructure with thin-walls and relatively uniform pore size, (2) Evolution of pre-existing pores in the sample during expansion; **b** Regions of interest (yellow squares) in the X-ray CT slices of samples fried at 150 °C: (1) Transformation of the dense sample into a highly porous microstructure with small and large pores supported by thin-walls, (2) Evolution of pre-existing pores in the sample during expansion subsequently compressed by continued expansion of internal regions; (3) Formation of the thick crust subsequently comprising of small pores compressed under internal expansion. Scale bars indicated in µm; time labels f_i denote observations during deep-frying period, subscripts denote the time in seconds.

projection imaging are showing promise in capturing ultra-fast phenomenon[66].

Third, oil uptake that may be occurring in the small nano-pores remains undetectable at current voxel resolutions. This could be improved by using a more tailored setup and sample environment to enable higher sensitivity, contrast and spatial resolution, particularly with pink beam imaging[67]. While reliance on synchrotron light sources currently limits accessibility, rapid advances in lab-based systems and iterative reconstruction algorithms hold significant promise for broader application of this technique for similar applications in food processing[46,47].

Finally, the WFD model system represents a similar class of products (e.g., donuts, noodles). Applying this technique to more traditional potato-based products (e.g., French fries, potato chips) and breaded foods under varying experimental conditions will provide valuable insights transferable to other mass-consumed products. Food microstructure analysis using various imaging techniques has already contributed to significant advancements across different product types[68,69]. As in-situ imaging methods continue to evolve, they are likely to enable further breakthroughs. While the current limitations pose challenges, they also present opportunities for future improvements and innovations.

The large amounts of time series data generated during imaging make machine learning assisted segmentation indispensable for the processing and segmentation of the different phases for quantification of important parameters during post-frying cooling. Uncertainty in prediction maps during classification, especially at phase transition boundaries, is unavoidable. Validation steps, including visual cross-checks between segmented datasets and corresponding grey-scale images, with a human-in-the-loop during training, were applied to minimise errors. Advances in deep learning algorithms for segmentation of large imaging datasets are expected to further improve segmentation accuracy[70]. Moreover, µCT image analysis offers distinct advantages over traditional methods such as nitrogen adsorption (NAM) and mercury intrusion porosimetry (MIP) for evaluating pore characteristics. These techniques require extensive sample preparation, including degassing and removal of oil and moisture, which can induce irreversible changes to the sample microstructure (e.g., shrinkage), potentially leading to discrepancies in measured values. NAM is effective for detecting nanopores but is not suited for characterising larger pores (>500 nm)[71], while MIP, although useful for analysing larger pores (0.2–250 µm), requires high pressures for effective mercury intrusion, that can potentially damage the samples[72]. In contrast, several studies have shown that image analysis (µCT) yields results comparable to traditional analytical methods, with no significant differences in oil content and porosity measurements[45,71,73], confirming the reliability and accuracy of image processing for characterising these porous structures.

We were able to confirm a number of pre-existing theories related to the process, (1) continually escaping gases significantly impede oil uptake during deep-frying[4,31]; (2) higher oil temperature, and, consequently more extensive moisture loss, during deep-frying results in

higher oil uptake[2,30]; and (3) the rising trend of oil uptake during post-frying cooling[23,74]. Combined with complementary tests for moisture content and temperature measurements, the present investigation provides additional insights into these underlying theories. Capillary action within the small crust pores was the primary driver of oil absorption during cooling, with vapour condensation further contributing to oil uptake as temperatures drop below 100 °C. The formation of a distinct crust in samples deep-fried at 180 °C and 150 °C was more conducive for oil uptake due to surface openings in a deformed microstructure. Differences in structural transformation (of starch and protein constituents) due to differing rates of moisture loss from heat conduction within the samples contributed to the distinctly different oil uptake rates and oil distribution inside the microstructure. For samples deep-fried at 120 °C, limited deformation during deep-frying resulted in a significantly lower final oil content due to reduced connectivity of the collapsed pore-space during cooling.

Pore connectivity analysis revealed that oil primarily filled the smaller pores in the crust regions, with restrained penetration into the core due to limited pore network connectivity and intact wall networks. However, current models lack the capability to accurately reflect changes in pore structural properties during deep-frying. The integration of 4D µCT is expected to significantly enhance the existing modelling framework[75] by providing high-resolution, time-resolved imaging of the dynamic changes in food microstructures and oil uptake. Equivalent pore network models (PNM) generated using segmented CT images to capture pore space geometry, have shown great promise in simulating multiphase flow at the microscale[53]. These models similarly can be used to simulate dynamic multiphase flow and study oil imbibition while incorporating the effects of varying pore morphologies. This can lead to improved precision in macroscale and porous media models, resulting in better predictions of oil, water, and vapour transport, thereby optimising the deep-frying process.

Deep-frying not only induces physicochemical changes in food components but also in the frying medium (oil) as oil degradation has been linked to frying duration and temperature[76]. Moreover, it is well established that the formation of acrylamide, a compound classified as a probable human carcinogen by the International Agency for Research on Cancer, accelerates at temperatures above 120 °C[7,77]. While this has prompted the adoption of several pretreatment techniques (e.g., pulsed electric field, ultrasound, radiofrequency, etc.)[78] and modified frying processes at lower temperatures (e.g., par-frying and vacuum frying)[21,79], the exact influence on the product microstructure and dynamics of oil uptake remains unclear. 4D µCT imaging can be employed to assess the effectiveness of the different pre-processing techniques in products undergoing deep-frying operations to assist with the interpretation and control of oil uptake.

Broadly, this study underscores that oil ingress can be linked to several interdependent factors, such as the rate of moisture loss, frying temperature, pore connectivity to the food surface, and structural rigidity. This presents new evidence that complements earlier results and provides new avenues for understanding and optimising deep-frying processes. To build further on this work, a multifaceted approach is advised to gain a better understanding of the relationship between deep-frying temperature and sensory and nutritional properties of the product. Furthermore, future investigations to gain insights into how other factors (e.g., food formulations, oil types, physicochemical properties of carbohydrate or protein constituents etc.) contribute to pore network connectivity are recommended as high-resolution, time-resolved imaging methods become more accessible.

Methods

Materials

Wheat flour (14.1% moisture content and 11.5% protein content) was purchased from Molens Vanden Bempt (Sint-Joris-Weert, Belgium). To 400 g flour, 175 mL deionized water was added. After a 15 min rest, the dough was kneaded for 15 min using a Panasonic (Kadoma, Osaka, Japan) SD-25511WXE automated bread maker and rested for 70 min. Samples (50 mg DM basis) further referred to as WFD (wheat flour dough containing 40% water) were withdrawn and shaped to fit inside the sample holder (TSC) before deep-frying. Sunflower frying oil was obtained from Agristo (Nazareth, Belgium), and was chosen as a frying medium due to its popularity in industrial deep-frying applications. Cylindrical TSCs were machined from Polytetrafluoroethylene (PTFE) rods in a standard configuration of 5.5 mm internal diameter and 18 mm high, with ≈20% open surface area through 115–120 perforations with a diameter of 0.7 mm along the surface and 17 perforations with a diameter of 0.3 mm at the bottom to allow easy exchange of fluids during deep-frying (see Supplementary Fig. 8a, b).

Experiment setup

A custom experiment setup was developed to remotely manipulate the sample in-situ during deep-frying and post-frying cooling using the synchrotron imaging setup (Fig. 1a). Frying oil was added to a round bottom flask with three parallel necks (500 mL, Lenz Laborglas, Wertheim, Germany); to heat and maintain the temperature of frying oil (logged using a J- type thermocouple, see Supplementary Fig. 8c), a heating mantle (WHM12033, witeg Labortechnik, Wertheim, Germany) with built-in stirring was mounted securely to the precision rotation stage. Vertical movement of the sample (to lower the sample into hot oil for deep-frying and retract the sample from oil after deep-frying) was facilitated using a linear actuator (8-inch stroke, Firgelli Automations, Ferndale, WA, USA) with a custom machined aluminium coupler (Fig. 1b) to allow interchanging TSCs between acquisitions without disturbing the setup. The stroke length for extension (ensuring full immersion of the sample holder in hot oil) and retraction of actuator shaft was controlled using a timer set at 7 s. To keep the sample stable and within the field of view (FOV) during tomography, the actuator was aligned with the axis of rotation and the central neck of the flask using an aluminium support rod (12.5 mm diameter) threaded to the mounting plate. Thermocouple and actuator signals were transmitted through a slip-ring in the rotation stage, facilitating remote operation of sample movement from the control hutch.

Deep-frying and post-frying processes

Before every acquisition, the frying oil was heated uniformly to T_{oil} + 5 °C (where, T_{oil} is the temperature of oil at 180, 150 or 120 °C). The prepared sample was carefully placed in the TSC. Next, the TSC was securely attached to the actuator coupler, and, subsequently, the heating mantle was unplugged to allow free rotation of the experimental stage; in offline tests it was confirmed that the residual heat in the heating mantle was sufficient to maintain the required temperature of the oil. After completion of necessary beamline safety procedures to secure the experiment hutch (ca. 1 min), the rotation stage was brought up to the required speed and actuator shaft was remotely extended into the frying oil. Once the sample was completely immersed in oil and stationary (ca. 1 s in oil) the acquisition protocol was initiated, with the first time point beginning at the first captured tomograph (Fig. 1d). For imaging the post-frying phase, the first part followed the same steps as deep-frying. The samples were fried for the duration of 56 s, after which the actuator shaft was retracted from the oil to its starting position. The acquisition protocol began once the shaft was stationary, and the sample was in the FOV (a delay of about 7 s had to be included between the sample being extracted from the oil to a stationary state and the first captured tomograph). Each sample was evaluated in triplicate for both deep-frying and the post-frying processes.

In-situ time-resolved synchrotron radiation tomography

A filtered broad-spectrum X-ray beam provided by a wiggler insertion device was used to provide sufficiently high photon-flux density in the ID19 beamline experimental hutch located 150 m from the source[80].

Along the vacuum flight tube (i.e., between the source and the experimental hutch), the beam was conditioned with two sets of white-beam slits, primary slits at 40 m from the source for heat load moderation and secondary slits for beam collimation located 140 m from the source, as well as a series of attenuators for optimisation of the on-sample spectrum. The beam exposure induced heating on the sample was considered to be negligible due to the pre-existing condition of immersion in hot oil. After impinging the fast rotating sample, the transmitted beam was detected with an indirect detector assembly consisting of a scintillator, a folding mirror, objective lens and a fast sCMOS camera[81]. Two configurations for fast in-situ tomographic visualization of the deep-frying and post-frying processes were utilised. For in-situ tracking of the pore formation during nucleation stage of the deep-frying process, the beam was conditioned with 1.4 mm aluminium and 0.8 mm diamond attenuators providing a peak energy of 30 keV. The fast indirect detector positioned 1 m away from the sample consisted of a 5× objective lens Mitutoyo (Kanagawa, Japan) Plan Apo (NA = 0.14) with a 250 μm LuAG:Ce scintillator providing a resulting voxel size of 2.2 μm and total FOV of 4.43 mm × 4.43 mm. For the visualization of the post-frying cooling process the beam passed through 1.4 mm aluminium, 0.14 mm copper and 0.8 mm diamond attenuators providing a peak energy of 35 keV. The fast indirect detector positioned 7 m away from the sample consisted of a 2× objective tandem lens (210:100 mm Hasselblad) with a 500 μm LuAG:Ce scintillator providing a voxel size of 5.2 μm and cylindrical FOV of 11 mm × 8.25 mm. This visualization of the cooling process was performed at a wider FOV to visualise the sample in its entirety and to obtain a contextual reference for evaluating oil uptake patterns. For both setups, the optical signal converted from the scintillator was captured using a sCMOS camera-type pco.dimax (S7, PCO AG, Germany) with a pixel count per frame of 2016 × 2016 pixels, having a 11 μm on-sensor pixel size and onboard memory. To capture the dynamic process at a representative temporal sampling, acquisitions were performed at fixed time intervals due to the limited onboard memory. Six full tomographs were acquired for each acquisition at 1 tomograph per second (1000 radiographs at 1 ms exposure over 360° for each tomograph). The time spacing between each tomograph was kept at 10 s during deep-frying (denoted by 1, 12, …, 56 s) and post-frying process (denoted by 8, 19, …, 63 s). An additional set of observations were performed at 3 s interval spacing (denoted by 1, 5, …, 21 s) to visualise the nucleation stage during the deep-frying process for samples fried at 180 °C. Finally, to establish a reference for sample microstructure, hydrated prepared samples were placed in micro-centrifuge tubes and imaged at 2.2 μm pixel resolution using a UniTom HR X-ray μCT scanner (TESCAN XRE, Ghent, Belgium) following the acquisition protocol described in Riley et al.[14].

Image processing and analysis

Image reconstruction was performed with the gold-standard filtered-back projection algorithm incorporating single distance phase retrieval[82] using in-house developed software, Tomwer v1.0.0 (https://gitlab.esrf.fr/tomotools/tomwer). The 3D topographies for each acquisition time point were reconstructed taking into account parameters such as centre-of-rotation alignment, single material complex refraction index ratio [delta/beta = 1000 (frying), 6000 (post-frying)] and ring artefact removal to obtain cross-section image stacks of 3D distribution of material phases. The transmitted beam detected by the detector assembly was attenuated not just by the individual sample constituents, but also by the borosilicate glass (flask) and a significant volume of hot frying oil. Owing to propagation-based phase contrast contribution thanks to (partial)spatial coherence of the impinging radiation, sufficient sensitivity was obtained to distinguish between four different phases within the 3D reconstructed phase fields: gas, oil, sample, TSC. Subsequently, images were imported in Avizo 3D 2021.2 (FEI Thermo Fisher Scientific, Waltham, MA, USA) for further image processing. The reconstructed 32-bit volumes were cast as 16-bit considering 1% – 99% intensity values in the volume histogram to subsequently characterise the phases of interest. Following this, a 3D non-local means filter was applied to denoise the image while preserving thin structures.

As individual phases affected the absorption characteristics of X-rays, phases were characterised using their respective intensity values based on their distinct attenuation characteristics arising from differences in atomic number and density along with spatial and temporal context from time-series data at different stages during acquisition[83,84]. For example, from the images and grey intensity histograms in Fig. 1d we identified oil in contact with the sample inside the TSC at f_{1s} followed by subsequent expulsion of oil in later timepoints f_{34s} and used the corresponding attenuation coefficient to identify oil in the sample. The order of greyscale intensities (from bright to dark) followed TSC > solid > oil > gas. Here, the solid structure corresponds to the (deep-fried) WFD including starch-gluten-water as the interaction between the components changed during the process. It was previously demonstrated using lab-based μCT that the starch-water solid structure indeed exhibited higher X-ray attenuation than oil and air[14]. As most of the water was bound by the starch and gluten components in the hydrated WFD sample, only a small proportion of free water would have been available[33,85]. During deep-frying, the phase conversion of water to vapour would further render the identification of water difficult as the moisture content continuously reduced during the process (Fig. 4a). Therefore, it was not possible to identify and segment water from the solid. Other authors confirmed the challenge of separating water from the solid structure due to their similarity of effective atomic number (Z_{eff})[73]. Due to extensive structural deformation of the sample matrix during deep-frying, certain regions underwent rapid expansion, faster than the acquisition rate leading to localised motion artefacts during reconstruction. Consequently, reliable segmentation of the acquisitions during deep-frying was not possible. Figure 1d provides an example of histogram shift during the deep-frying process as the structure deforms, the coloured regions highlight the intensity values corresponding to the different phases. Due to the inherent properties of CT acquisition, the reconstructed images are prone to gaussian noise or sub-pixel effects, thus some overlap between the intensity of the phases is to be expected. Identifiable microstructural features such as individual phases, porosity, connected pores were characterised typically based on at least double the scanned voxel size of the image[47,86].

Conversely, sample deformation was limited for the post-frying process and did not influence the segmentation. This was performed with the help of machine learning assisted pixel classification in Ilastik v1.4.0[60]. Sparse manual annotations were marked based on spatial context and greyscale intensities across 10% of the reconstructed images (150 cross-sectional slices) for each timestep and for each sample group from the different deep-frying temperatures (180, 150 and 120 °C) as training data for the random forest classifier to label pixels into four classes: oil, gas, solid and TSC. The models were trained iteratively to reduce the uncertainty between classes and reduce out-of-bag (OOB) error (available in Supplementary Table 2) for the annotated pixels. As the classifier is susceptible to a higher uncertainty in regions of phase transition (i.e., boundary of two labels) compared to homogeneous parts[60], an additional error (ca. 5.5% – 8.5%) across the datasets was found in terms of class label total volumes, mainly attributed to pore-cell wall transitions. Corresponding probability maps were segmented using a global threshold set to 0.5 in MATLAB (version 2019b, MathWorks, Natick, MA, USA). In regions of high uncertainty, the probability of a pixel corresponding to either class was below 0.5, in these particular cases the pixels were left unassigned for the quantification. The segmented images stacks were then reimported in Avizo to perform several morphological operations (filter by measure, ambient occlusion etc.) to isolate the sample and

the oil inside the sample (image processing workflow presented in Fig. 5). The individual calculations of volume fraction of the three phases and porosities (total and gas) was conducted. The volume fraction of the distinct phases was calculated as:

$$\varepsilon_i = \frac{V_i}{V_{\text{total}}} \quad (1)$$

with ε_i the volume fraction of i-th phase (starch, oil, gas), V_i the volume of i-th phase, and V_{total} the total volume of the sample.

The volumetric oil contents inside solid matrix were calculated in two ways: first, as the ratio of the volume occupied by the oil phase (oil-filled pores) to the volume of both oil and starch phases; and second, as the ratio of the volume occupied by the oil phase (oil-filled pores) to the total characterised sample volume. Oil uptake in the small nanopores present in the crust region was not investigated to achieve a good balance for the acquisition protocol across acquisition rate, voxel resolution and FOV considerations. Furthermore, to evaluate the connectivity of oil-filled pores inside the solid matrix, the segmented oil phase was labelled following an opening operation to prevent effects of phase-transition artefacts[87]. The labelled pores were coloured based on the connectivity of adjacent components.

The total porosity (ϕ_{total}) was evaluated based on the pore volume occupied by oil (ε_{oil}) and gas (ε_{gas}):

$$\phi_{\text{total}} = \varepsilon_{\text{gas}} + \varepsilon_{\text{oil}} \quad (2)$$

The gas porosity of the non-fried samples was calculated across 3 representative volumes of $1.54 \times 1.54 \times 1.54$ mm^3.

To investigate the microstructural differences between the crust and core regions of the deep-fried samples, an outer layer with a constant thickness of 0.5 mm was separated at the surface using the chamfer distance map in Avizo. The crust and core regions were masked from the segmented dataset and pore size distribution was evaluated at 8 and 63 s during the post-frying cooling following a watershed separation.

The local structure thickness distribution (expressed in μm) of the starch-gluten matrix was evaluated for the sample and the separated crust and core regions using CTAn (Version 1.18.8.0, Bruker SkyScan, Kontich, Belgium). The sphere-fitting algorithm in the 3D analysis module provided the local thickness of the structure as represented by the diameter of the largest enclosed sphere[88].

Determination of moisture content

The moisture content of the WFD and deep-fried samples at 180, 150, or 120 °C for 5, 10, 15, 20, 30, 40, 50, and 60 s was evaluated using the AACC method 44–15.02[89]. Samples were deep-fried using the same experimental setup and cooled for 60 s before moisture content determination. The measurements were repeated for a total of six replicates for each of the time points. The moisture content was calculated on a dry matter basis [m_{H2O} ($m_{\text{dough DM}}$)$^{-1}$], where mass (m) is expressed in grams and DM indicates dry matter of the solids (excluding oil absorbed as a consequence of deep-frying).

Temperature measurements during deep-frying and post-frying

Temperature profiles inside the WFD samples during and after deep-frying were measured in the crust and core separately using a K-type thermocouple (0.075 mm probe diameter, RS-pro, London, UK) connected to a digital acquisition system (34970 A, Agilent Technologies, Santa Clara, CA, USA) recording data at a frequency of 2 Hz. The measurements in the crust and core regions were conducted near the surface for the crust (within 1 mm) and at the centre of the sample for the core (see Supplementary Fig. 9). Temperatures were logged continuously during deep-frying (56 s) and the post-frying (63 s) period, same as the 4D μCT imaging. At least five replicates were obtained for each deep-frying temperature 180, 150, or 120 °C to account for any variation in the placement of the thermocouple.

Statistical analysis

The results are expressed as mean and standard deviation of replicates. To determine whether the means were significantly different, a mixed model with one-way ANOVA was performed to determine the combined effect of frying temperature and time. A multiple comparisons test was performed using Tukey's honest significant difference for all pairwise comparisons with the level of significance set at $p < 0.05$. All statistical analyses were performed using JMP pro 17.2 (SAS Institute, Cary, NC, USA).

Reporting summary

Further information on research design is available in the Nature Portfolio Reporting Summary linked to this article.

Data availability

The data that support the findings of this study are available from the ESRF data portal[90], Zenodo[91], and from the corresponding author upon request.

References

1. Gamble, M. H., Rice, P. & Selman, J. D. Relationship between oil uptake and moisture loss during frying of potato slices from c. v. Record U.K. tubers. *Int. J. Food Sci. Technol.* **22**, 233–241 (1987).
2. Ziaiifar, A. M., Achir, N., Courtois, F., Trezzani, I. & Trystram, G. Review of mechanisms, conditions, and factors involved in the oil uptake phenomenon during the deep-fat frying process. *Int. J. Food Sci. Technol.* **43**, 1410–1423 (2008).
3. U.S. Department of Agriculture, A. R. S. *USDA Food and Nutrient Database for Dietary Studies 2019-2020*. (2022).
4. Dana, D. & Saguy, I. S. Review: Mechanism of oil uptake during deep-fat frying and the surfactant effect-theory and myth. *Adv. Colloid Interface Sci* **128–130**, 267–272 (2006).
5. Hooper, L. et al. Reduction in saturated fat intake for cardiovascular disease. *Cochrane Database Syst. Rev.* **2020**, (2020).
6. Hooper, L., Abdelhamid, A. S., Jimoh, O. F., Bunn, D. & Skeaff, C. M. Effects of total fat intake on body fatness in adults. *Cochrane Database Syst. Rev.* **2020**, CD013636 (2020).
7. Mottram, D. S., Wedzicha, B. L. & Dodson, A. T. Acrylamide is formed in the Maillard reaction. *Nature* **419**, 448–449 (2002).
8. World Health Organization. *Total Fat Intake for the Prevention of Unhealthy Weight Gain in Adults and Children*. (2023).
9. Pagliai, G. et al. Consumption of ultra-processed foods and health status: a systematic review and meta-analysis. *Br. J. Nutr.* **125**, 308–318 (2021).
10. Monteiro, C. A., Moubarac, J. -C., Cannon, G., Ng, S. W. & Popkin, B. Ultra-processed products are becoming dominant in the global food system. *Obes. Rev.* **14**, 21–28 (2013).
11. Vitrac, O., Trystram, G. & Raoult-Wack, A. L. Deep-fat frying of food: Heat and mass transfer, transformations and reactions inside the frying material. *Eur. J. Lipid Sci. Technol.* **102**, 529–538 (2000).
12. Moreira, R. G., Sun, X. & Chen, Y. Factors affecting oil uptake in tortilla chips in deep-fat frying. *J. Food Eng.* **31**, 485–498 (1997).
13. Alam, T. & Takhar, P. S. Microstructural characterization of fried potato disks using x-ray micro computed tomography. *J. Food Sci.* **81**, E651–E664 (2016).
14. Riley, I. M. et al. Impact of potato starch structural transitions on microstructure development during deep-frying. *Food Hydrocoll* **142**, 108833 (2023).
15. Bouchon, P., Aguilera, J. M. & Pyle, D. L. Structure Oil-Absorption Relationships during Deep-Fat Frying. *J. Food Sci.* **68**, 2711–2716 (2003).
16. Ufheil, G. & Escher, F. Dynamics of oil uptake during deep-fat frying of potato slices. *Lwt* **29**, 640–644 (1996).

17. Dueik, V., Moreno, M. C. & Bouchon, P. Microstructural approach to understand oil absorption during vacuum and atmospheric frying. *J. Food Eng.* **111**, 528–536 (2012).
18. Moreno, M. C., Brown, C. A. & Bouchon, P. Effect of food surface roughness on oil uptake by deep-fat fried products. *J. Food Eng.* **101**, 179–186 (2010).
19. Baumann, B. & Escher, F. Mass and heat transfer during deep-fat frying of potato slices -I. rate of drying and oil uptake. *LWT - Food Sci. Technol.* **28**, 395–403 (1995).
20. Albert, S. & Mittal, G. S. Comparative evaluation of edible coatings to reduce fat uptake in a deep-fried cereal product. *Food Res. Int.* **35**, 445–458 (2002).
21. Liberty, J. T., Dehghannya, J. & Ngadi, M. O. Effective strategies for reduction of oil content in deep-fat fried foods: A review. *Trends Food Sci. Technol.* **92**, 172–183 (2019).
22. Ziaiifar, A. M., Courtois, F. & Trystram, G. Porosity development and its effect on oil uptake during frying process. *J. Food Process Eng.* **33**, 191–212 (2010).
23. Halder, A., Dhall, A. & Datta, A. K. An improved, easily implementable, porous media based model for deep-fat frying. Part II: Results, validation and sensitivity analysis. *Food Bioprod. Process.* **85**, 220–230 (2007).
24. Zhang, J., Liu, Y. & Fan, L. Effect of pore characteristics on oil absorption behavior during frying of potato chips. *Innov. Food Sci. Emerg. Technol.* **66**, 102508 (2020).
25. Kalogianni, E. P. & Papastergiadis, E. Crust pore characteristics and their development during frying of French-fries. *J. Food Eng.* **120**, 175–182 (2014).
26. Moreira, R. G. & Barrufet, M. A. A new approach to describe oil absorption in fried foods: a simulation study. *J. Food Eng.* **35**, 1–22 (1998).
27. Zhang, T., Li, J., Ding, Z. & Fan, L. Effects of initial moisture content on the oil absorption behavior of potato chips during frying process. *Food Bioprocess Technol* **9**, 331–340 (2016).
28. Reyniers, S. et al. Amylose molecular fine structure dictates water–oil dynamics during deep-frying and the caloric density of potato crisps. *Nat. Food* **1**, 736–745 (2020).
29. Gazmuri, A. M. & Bouchon, P. Analysis of wheat gluten and starch matrices during deep-fat frying. *Food Chem* **115**, 999–1005 (2009).
30. Liu, Y., Tian, J., Zhang, T. & Fan, L. Effects of frying temperature and pore profile on the oil absorption behavior of fried potato chips. *Food Chem* **345**, 128832 (2021).
31. Touffet, M., Trystram, G. & Vitrac, O. Revisiting the mechanisms of oil uptake during deep-frying. *Food Bioprod. Process.* **123**, 14–30 (2020).
32. Jekle, M., Mühlberger, K. & Becker, T. Starch-gluten interactions during gelatinization and its functionality in dough like model systems. *Food Hydrocoll* **54**, 196–201 (2016).
33. Thanatuksorn, P., Kajiwara, K. & Suzuki, T. Characterization of deep-fat frying in a wheat flour–water mixture model using a state diagram. *J. Sci. Food Agric.* **87**, 2648–2656 (2007).
34. Wang, Z. et al. Effects of thermal properties and behavior of wheat starch and gluten on their interaction: a review. *Int. J. Biol. Macromol.* **177**, 474–484 (2021).
35. Chen, L. et al. Comprehensive investigation and comparison of surface microstructure of fractionated potato starches. *Food Hydrocoll* **89**, 11–19 (2019).
36. Li, W. et al. Low and high methoxyl pectin lowers on structural change and digestibility of fried potato starch. *LWT* **132**, 109853 (2020).
37. Aguilera, J. M., Cadoche, L., Loópez, C. & Gutierrez, G. Microstructural changes of potato cells and starch granules heated in oil. *Food Res. Int.* **34**, 939–947 (2001).
38. Kawas, M. L. & Moreira, R. G. Characterization of product quality attributes of tortilla chips during the frying process. *J. Food Eng.* **47**, 97–107 (2001).
39. Bouchon, P. & Aguilera, J. M. Microstructural analysis of frying potatoes. *Int. J. Food Sci. Technol.* **36**, 669–676 (2001).
40. Dhital, S., Baier, S. K., Gidley, M. J. & Stokes, J. R. Microstructural properties of potato chips. *Food Struct* **16**, 17–26 (2018).
41. Aguilera, J. M. Why food micro structure? *J. Food Eng.* **67**, 3–11 (2005).
42. Dehghannya, J. & Ngadi, M. Recent advances in microstructure characterization of fried foods: different frying techniques and process modeling. *Trends Food Sci. Technol.* **116**, 786–801 (2021).
43. Yang, D., Wu, G., Li, P., Zhang, H. & Qi, X. Comparative analysis of the oil absorption behavior and microstructural changes of fresh and pre-frozen potato strips during frying via MRI, SEM, and XRD. *Food Res. Int.* **122**, 295–302 (2019).
44. Li, P. et al. Effect of multistage process on the quality, water and oil distribution and microstructure of French fries. *Food Res. Int.* **137**, 109229 (2020).
45. Contardo, I., James, B. & Bouchon, P. Microstructural characterization of vacuum-fried matrices and their influence on starch digestion. *Food Struct* **25**, 100146 (2020).
46. Dewanckele, J., Boone, M. A., Coppens, F., van Loo, D. & Merkle, A. P. Innovations in laboratory-based dynamic micro-CT to accelerate in situ research. *J. Microsc.* **277**, 197–209 (2020).
47. Withers, P. J. et al. X-ray computed tomography. *Nat. Rev. Methods Prim.* **1**, 18 (2021).
48. Turbin-Orger, A. et al. Growth and setting of gas bubbles in a viscoelastic matrix imaged by X-ray microtomography: The evolution of cellular structures in fermenting wheat flour dough. *Soft Matter* **11**, 3373–3384 (2015).
49. Schott, F. et al. Structural formation during bread baking in a combined microwave-convective oven determined by sub-second in-situ synchrotron X-ray microtomography. *Food Res. Int.* **173**, 113283 (2023).
50. Gruber, S. et al. Pore shape matters – In-situ investigation of freeze-drying kinetics by 4D XCT methods. *Food Res. Int.* **193**, 114837 (2024).
51. Patsioura, A. et al. Microscopic imaging of biphasic oil-air flow in <scp>F</scp> rench fries using synchrotron radiation. *AIChE J.* **61**, 1427–1446 (2015).
52. Blankenburg, C., Rack, A., Daul, C. & Ohser, J. Torsion estimation of particle paths through porous media observed by in-situ time-resolved microtomography. *J. Microsc.* **266**, 141–152 (2017).
53. Piovesan, A. et al. 4D synchrotron microtomography and pore-network modelling for direct in situ capillary flow visualization in 3D printed microfluidic channels. *Lab Chip* **20**, 2403–2411 (2020).
54. Delcour, J. A. & Hoseney, R. C. *Principles of Cereal Science and Technology*. (AACC International, 2010).
55. Farkas, B. E., Singh, R. P. & Rumsey, T. R. Modeling heat and mass transfer in immersion frying. I, model development. *J. Food Eng.* **29**, 211–226 (1996).
56. Mondal, A. & Datta, A. K. Bread baking - A review. *J. Food Eng.* **86**, 465–474 (2008).
57. Ni, H. & Datta, A. K. Moisture, oil and energy transport during deep-fat frying of food materials. *Food Bioprod. Process. Trans. Inst. Chem. Eng. Part C* **77**, 194–204 (1999).
58. Reyniers, S., Ooms, N. & Delcour, J. A. Transformations and functional role of starch during potato crisp making: A review. *J. Food Sci.* **85**, 4118–4129 (2020).
59. Riley, I. M., Verma, U., Verboven, P., Nicolai, B. M. & Delcour, J. A. Wheat gluten structure and (non–)covalent network formation during deep-fat frying. *Food Res. Int.* **188**, 114503 (2024).
60. Berg, S. et al. Ilastik: interactive machine learning for (Bio)image analysis. *Nat. Methods* **16**, 1226–1232 (2019).
61. Sandhu, J., Bansal, H. & Takhar, P. S. Experimental measurement of physical pressure in foods during frying. *J. Food Eng.* **115**, 272–277 (2013).

62. HUBBARD, L. J. & FARKAS, B. E. Influence of oil temperature on convective heat transfer during immersion frying. *J. Food Process. Preserv.* **24**, 143–162 (2000).
63. van der Sman, R. G. M. & van der Goot, A. J. The science of food structuring. *Soft Matter* **5**, 501–510 (2009).
64. Tengattini, A. et al. NeXT-Grenoble, the Neutron and X-ray tomograph in Grenoble. *Nucl. Instruments Methods Phys. Res. Sect. A Accel. Spectrometers, Detect. Assoc. Equip.* **968**, 163939 (2020).
65. Nemati, A., Lukić, B., Tengattini, A., Briffaut, M. & Séchet, P. Water vapor condensation in porous media: effects of fracture, porosity, and flow rate revealed by rapid 4D neutron imaging. *Adv. Water Resour.* **195**, 104872 (2025).
66. Asimakopoulou, E. M. et al. Development towards high-resolution kHz-speed rotation-free volumetric imaging. *Opt. Express* **32**, 4413 (2024).
67. Mittone, A. et al. Multiscale pink-beam microCT imaging at the ESRF-ID17 biomedical beamline. *J. Synchrotron Radiat.* **27**, 1347–1357 (2020).
68. Aguilera, J. M. Food structure revisited. *Trends Food Sci. Technol.* **147**, 104459 (2024).
69. Schoeman, L., Williams, P., du Plessis, A. & Manley, M. X-ray micro-computed tomography (μCT) for non-destructive characterisation of food microstructure. *Trends Food Sci. Technol.* **47**, 10–24 (2016).
70. Archana, R. & Jeevaraj, P. S. E. Deep learning models for digital image processing: a review. *Artif. Intell. Rev.* **57**, 11 (2024).
71. Zhang, J., Li, J. & Fan, L. Comparative analysis of oil absorption and microstructure of fried potato chips treated with different pre-treatment via X-ray micro-computed tomography and mercury intrusion method. *J. Food Compos. Anal.* **129**, 106129 (2024).
72. Xue, S. et al. Comparison of mercury intrusion porosimetry and multi-scale X-ray CT on characterizing the microstructure of heat-treated cement mortar. *Mater. Charact.* **160**, 110085 (2020).
73. Contardo, I. & Bouchon, P. Enhancing Micro-CT methods to quantify oil content and porosity in starch-gluten matrices. *J. Food Eng.* **237**, 154–161 (2018).
74. Bouchon, P. & Pyle, D. L. Modelling oil absorption during post-frying cooling II: solution of the mathematical model, model testing and simulations. *Food Bioprod. Process.* **83**, 261–272 (2005).
75. Datta, A. et al. Computer-aided food engineering. *Nat. Food* **3**, 894–904 (2022).
76. Aladedunye, F. A. & Przybylski, R. Degradation and Nutritional Quality Changes of Oil During Frying. *J. Am. Oil Chem. Soc.* **86**, 149–156 (2009).
77. EFSA Panel on Contaminants in the Food Chain. Scientific Opinion on acrylamide in food. *EFSA J.* **13**, (2015).
78. Zhang, J., Li, J. & Fan, L. Application of innovative techniques in modifying microstructures and reducing oil uptake of fried food: A review. *Food Res. Int.* **196**, 115049 (2024).
79. Kumari, A., Bhattacharya, B., Agarwal, T., Paul, V. & Chakkaravarthi, S. Integrated approach towards acrylamide reduction in potato-based snacks: A critical review. *Food Res. Int.* **156**, 111172 (2022).
80. Weitkamp, T. et al. Status and evolution of the ESRF beamline ID19. in *X-ray Optics and Microanalysis: Proceedings of the 20th International Congress* 33–38 (AIP Publishing, Karlsruhe, 2010).
81. Douissard, P. A. et al. A versatile indirect detector design for hard X-ray microimaging. *J. Instrum.* **7**, P09016–P09016 (2012).
82. Paganin, D., Mayo, S. C., Gureyev, T. E., Miller, P. R. & Wilkins, S. W. Simultaneous phase and amplitude extraction from a single defocused image of a homogeneous object. *J. Microsc.* **206**, 33–40 (2002).
83. Jackson, D. F. & Hawkes, D. J. X-ray attenuation coefficients of elements and mixtures. *Phys. Rep.* **70**, 169–233 (1981).
84. Maire, E. & Withers, P. J. Quantitative X-ray tomography. *Int. Mater. Rev.* **59**, 1–43 (2014).
85. Riley, I. M., Nivelle, M. A., Ooms, N. & Delcour, J. A. The use of time domain 1 H NMR to study proton dynamics in starch-rich foods: A review. *Compr. Rev. Food Sci. Food Saf.* **21**, 4738–4775 (2022).
86. Schlüter, S., Sheppard, A., Brown, K. & Wildenschild, D. Image processing of multiphase images obtained via X-ray microtomography: A review. *Water Resour. Res.* **50**, 3615–3639 (2014).
87. Kerckhofs, G., Schrooten, J., Van Cleynenbreugel, T., Lomov, S. V. & Wevers, M. Validation of x-ray microfocus computed tomography as an imaging tool for porous structures. *Rev. Sci. Instrum.* **79**, 013711 (2008).
88. Hildebrand, T. & Rüegsegger, P. A new method for the model-independent assessment of thickness in three-dimensional images. *J. Microsc.* **185**, 67–75 (1997).
89. Moisture-Air-Oven Methods. in *AACC International Approved Methods* (AACC International, 2009).
90. Verma, U., Riley, I. M., Verboven, P. & Nicolaï, B. M. In situ visualization of fluid flow during deep-fat frying process using ultrafast synchrotron microtomography. *ERSF data repository* https://doi.org/10.15151/ESRF-ES-930328408 (2025).
91. Verma, U., Riley, I. M., Verboven, P. & Nicolaï, B. M. Supporting data. *Zenodo* https://doi.org/10.5281/zenodo.14507722 (2025).

Acknowledgements

FWO-Vlaanderen is acknowledged for funding the research project grant G.0903.19 N. The authors acknowledge the European Synchrotron Radiation Facility for provision of beamtime at beamline ID19 under the proposal 'LS-3126'. Alexander Rack and Marta Majkut (beamline scientists, ID19 ESRF) for their valuable advice related to the proposal and fruitful discussions related to experimental considerations during setup testing, respectively. The authors are also grateful to Gert van Beneden, Yves Severeyns and Riet Ramaekers (from CMW, CDE, KU Leuven respectively) for their assistance with specific individual components of the experimental setup.

Author contributions

B.M.N., P.V. and J.A.D. supervised the project. U.V., P.V. and B.M.N. conceptualised the work and applied for beamtime at ESRF. U.V. designed the experiment setup. I.M.R. designed and optimised the sample formulation. U.V., I.M.R., P.V. and B.M.N. conducted the synchrotron microtomographic experiment with help from B.L. and L.B. setting up the beamline at ESRF. U.V. processed the X-ray imaging data. All authors interpreted and discussed the results. U.V. prepared the original manuscript draft. All authors contributed to reviewing and editing the manuscript.

Competing interests

The authors declare no competing interests.

Additional information

Supplementary information The online version contains supplementary material available at https://doi.org/10.1038/s41467-025-57934-z.

Correspondence and requests for materials should be addressed to P. Verboven.

Peer review information *Nature Communications* thanks Pedro Bouchon, Liuping Fan and the other, anonymous, reviewer(s) for their contribution to the peer review of this work. A peer review file is available.